Master's thesis

NTNU
Norwegian University of Science and Technology
Faculty of Information Technology and Electrical Engineering
Department of Electronic Systems

Sofia Olivia Kathea Godø

Development of a Data Characterization Software for a Gamma Spectroscopy System

Master's thesis in Signal Processing & Communication

January 2021

NTNU
Norwegian University of Science and Technology

Sofia Olivia Kathea Godø

Development of a Data Characterization Software for a Gamma Spectroscopy System

Master's thesis in Signal Processing & Communication
January 2021

Norwegian University of Science and Technology
Faculty of Information Technology and Electrical Engineering
Department of Electronic Systems

NTNU
Norwegian University of
Science and Technology

Title: TBD
Student: Sofia Olivia Kathea Godø

Problem Description

IDEAS has developed a system using their own ASIC design for reading out CZT radiation detectors, which will be used to carry out gamma ray spectroscopy. Within this master thesis a calibration routine for this readout system shall be implemented in software. The routine shall be verified by obtaining spectra with radioactive sources and determining their quality based on the resulting spectral resolution. Methods for characterizing the data and improving spectral resolution shall also be considered for implementation. Effort shall be made to simplify the user experience, making a one-click calibration method that carries out the routine and produces the relevant reports.

Assignment Proposer: Arne Olav Gurvin Fredriksen, IDEAS
Supervisor: Giampiero Salvi, NTNU

Abstract

A system for carrying out CZT radiation spectrometer readouts from multiple CZT-crystals in parallel has been developed by the company IDEAS with their own ASIC, the IDE3421. The GDS-100 system requires a software that implements a calibration routine, and simplifies the user experience by translating the raw-binary file that the system provides into a spectrum in close to real-time. The software is also required to have analytical features for the data.

This thesis focuses on the necessary steps to develop a calibration routine, a user interface layout and development, as well as integration into already existing read-out software. The performance of the calibration routine is presented and analytical features are evaluated. Additional efforts to improve spectral resolution with depth interaction correction are explored and presented.

The *GDS-100 Calibration User Interface* was developed and the calibration routine performance was tested with radioactive source data. The best spectrum outcome was for single interaction events of Cs^{137} with a FWHM: 0.775%. Depth interaction correction using C/A-ratio gave a spectral resolution improvement from FWHM: 1.020% to FWHM: 0.880%.

Abstrakt

Basert på egen ASIC, IDE3421, har selskapet IDEAS utviklet et system som tolker spektrometeravlesninger fra flere parallelle CZT-krystaller. GDS-100-systemet har nytte av en programvare som implementerer en kalibreringsprosedyre som gjør det enklere for brukeren ved å oversette binær rådata systemet produserer til et energi spektrum tett opp mot sanntid. Programvaren trenger også egenskaper for dataanalyse og -forbedring.

Denne oppgaven omfatter utvikling av en kalibreringsprosedyre, utforming og utvikling av et funksjonelt brukergrensesnitt, og integrering av prosedyren i et dataprogram for avlesning. Ytelsen blir dokumentert, og analyseegenskaper evaluert. Ytterligere tiltak for høyere spektraloppløsning med korrigering for dybdeinteraksjon, blir undersøkt og forevist.

Brukergrensesnittet for kalibrering av systemet GDS-100 ble utviklet, og kalibreringsprosedyren ble testet. Det beste spektralresultatet for Cs^{137} ble målt til FWHM: 0.775%, for enkeltstående interaksjonshendelser. Korreksjon av dybdeinteraksjon med C/A-rate ga en forbedring av spektraloppløsning av Cs^{137} fra FWHM: 1.020% til FWHM: 0.880%.

Preface

The specialization project in the ninth semester at NTNU, was done in cooperation with the company Integrated Detector Electronics AS(IDEAS). The success of that project resulted in a natural further cooperation with this thesis. IDEAS is developing a new system with the same Application Specific Integrated Circuit(ASIC) as the system used in the specialization project. This meant I could bring all the experience working on the old system into creating a calibration software and user interface for this new system.

Even though the earlier experience gave me head start in knowing what would be required of this software, it brought a whole new aspect of actually developing a user interface from scratch. With no prior experience in designing and creating a user interface it brought a steep learning curve. Another challenge was a delay in delivery of system components as well as firmware development due to Covid-19. Even though this did limit some of the final testing, it did mean the software could be used in a practical sense to aid the development, which both helped to speed up the development but also to test the user interface.

This project required a large amount of laboratory work and close communication with the IDEAS employees. Hence, I decided to move to Oslo for the entire time frame of the project.

Overall, the project was a great experience and I would like to say a big thank you to the employees at IDEAS for treating me as one of their own. A special thank you go to Tor Magnus Johansen and Dirk Meier for sharing their vast knowledge and lastly a huge thank you to Arne Olav Gurvin Fredriksen who walked next to me during the whole process and guided me in the right direction.

Sofia Olivia Kathea Godø

Contents

List of Tables

List of Figures

Acronyms

ADC Analog Digital Converter

AMEGO All-sky Medium Energy Gamma-ray Observatory

ASIC Application Specific Integrated Circuit

Cs Cesium

CZT Cadmium Zinc Telluride

FPGA Field-Programmable Gate Array

FWHM Full Width Half Maximum

HV High Voltage

ID Identity Document

Na Sodium

NASA National Aeronautics and Space Administration

1 Introduction

Integrated Detector Electronics AS (IDEAS) has developed an Application Specific Integrated Circuit (ASIC) for reading out Cadmium Zing Telluride(CZT) radiation spectrometers, which is being considered for space mission ALL-sky Medium Energy Gamma-ray Observatory(AMEGO) proposed by National Aeronautics and Space Administration(NASA). The mission is a probe-class mission to provide ground-breaking new capabilities for multimessenger astrophysics in the under-explored gap of medium-energy gamma rays. Figure 1 displays a range of astrophysical objects that have unique signatures in the gamma-ray regime that will be further explored with the help of the AMEGO mission[2].

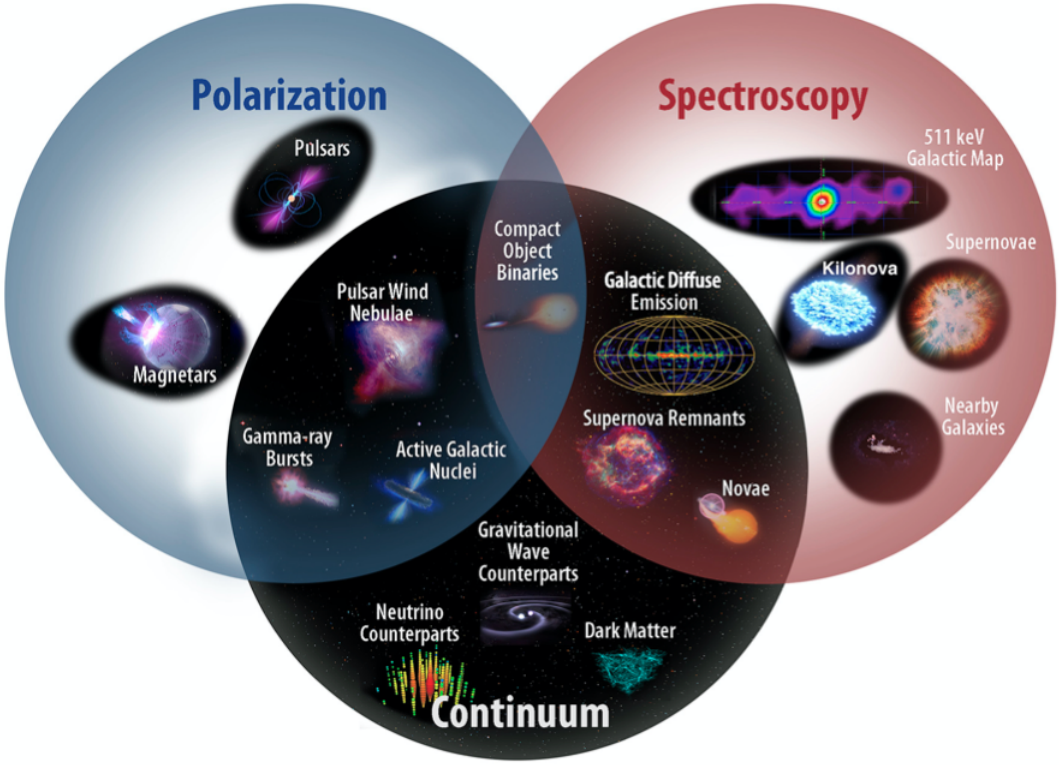

Figure 1 – AMEGO's main objectives of studies: A wide field of view and broad energy range will result in breakthroughs in time-domain and multi messenger astrophysics; polarization sensitivity will probe conditions and processes in astrophysical jets and in the magnetosphere and winds of compact objects; and nuclear line spectroscopy will provide insights into element formation in dynamic environments.

NASA is in the process of creating a prototype as a proof of concept, in order to strengthen the proposal for the mission to receive funding. IDEAS was chosen for their expertise and wast knowledge of gamma-radiation readout electronics, to create a system, the GSD-100, for multiple detector readout using the ASIC IDE3421, also developed by IDEAS. The system will be used in a beam test and potentially a balloon test. NASA will ultimately create their own customized software, but the goal of this project is to implement a user case for this system to provide insight into necessary calibrating and post processing steps.

The system provides the gamma radiation data in a raw binary format without corrections. In this format, the data is difficult to work with as well as time consuming for the user. This project is a continuation of a specialization project using the same ASIC, IDE3421, but in a single module readout system [1]. The main challenge in the specialization project was the time-consuming aspect of processing the data in order to analyze it. With experiences from the preceding project, as well as close collaboration with the system developers and physicists, a software was created to simplify this process. It is implemented as a user interface with features that effectively help the user identify errors as well as visualize important aspects of the system from a physics and system development point of view. The GDS-100 system was delayed and still under development in the majority of the projects time-frame. Consequently the software was also used as an analytical tool to aid the development, to identify errors and quantify possible weaknesses.

The software created is the *GDS-100 Calibration User Interface* which has two main purposes. It implements a calibration routine which characterizes and corrects any variations in baseline levels and gain. And it will showcase an instant result of the corrected data in close to real time, and how different configurations affect the data, so to simplify the user experience of the system. This thesis also makes additional efforts to create good-quality energy spectra of radioactive sources using depth interaction correction.

This report is mainly structured in the traditional IMRAD[1] way, however, the discussion section is divided between the software, testing, and depth correction, and is added to the end of each respective chapters for readability. Chapter 2 provides an introduction to the theory necessary for understanding the implementation. The chapter will give an introduction into gamma radiation, depth interaction correction and pulse height analysis. The following chapter will give a short overview of previous work, including results from the specialization project. Chapter 4 will present a system description and possible sources of error within the system along with necessary steps for correction. The next chapter introduce the *GDS-100 Calibration User Interface* with a description of its layout and features, as well as a discussion of the resulting software. Chapter 6 will provide testing of the software as well as the system itself. The laboratory setup is presented in the first section. The next section determines the linearity of the system. The third and fourth section will introduce the result followed by a discussion in the last section. The last chapter gives a summary which concludes this thesis.

[1]The IMRaD format is a standard for structuring a scientific article and is an acronym for Introduction, Method, Results, Discussion

2 Theory

2.1 Gamma Interactions

Gamma radiation is emitted by excited nuclei in their transition to lower lying nuclear layers. They are mass-less particles, *photons*, with energy essentially equal to the difference in energy between the initial and final nuclear states[3]. This energy can be detected as pulses by a radiation detector, and generate a distribution of pulse-heights. The distribution can be interpreted as a plot between the number of gamma ray pulses versus the energy from that radioactive source as depicted in Figure 2, i.e, a gamma ray spectrum. This section will explain the theory of the main gamma interactions with the resulting caveats they create in the energy spectrum, and how the CZT detector detects the energy pulses.

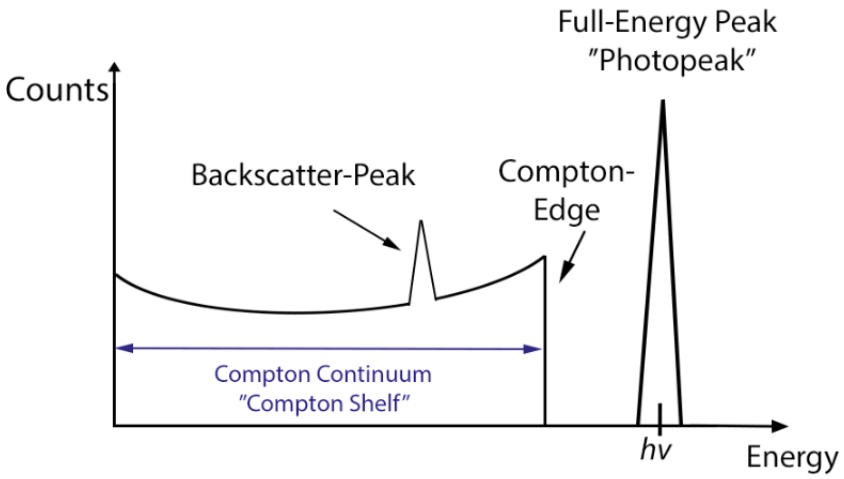

Figure 2 – An idealized γ-spectrum. The spectrum is composed of the full-energy peak and the Compton shelf.

Gamma rays have three interaction mechanisms when interacting with matter, which all lead to partial or complete transfer of gamma ray photon energy to electron energy. They are: *photoelectric absorption*, *Compton scattering*, and *pair production*. In photoelectric absorption the photon is completely absorbed by an absorber atom on which the atom ejects an energetic photoelectron, replacing the photons, with an energy of

$$E_{e^-} = hv - E_b \tag{1}$$

where E_b represent the binding energy of the photoelectron in its original shell, h Planck's constant and v the frequency of radiation events.

In Compton scattering, the gamma ray transfers parts of its energy to an electron and is deflected through an angle θ with respect to its original direction, as illustrated in Figure 3[12].

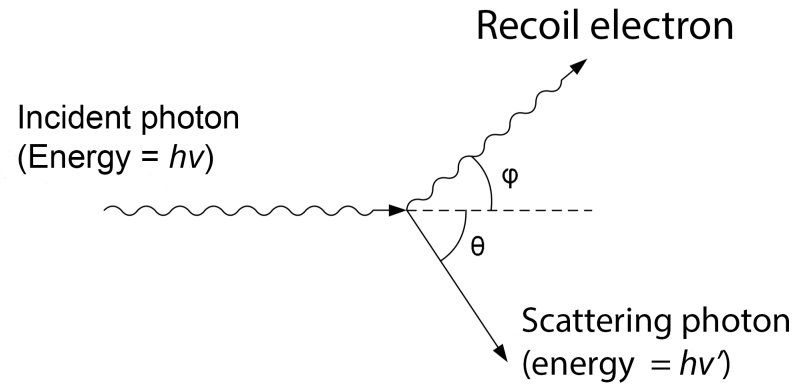

Figure 3 – A gamma ray Compton scattered by an electron.

Assuming the initial electron is at rest, the relationship between the scattered photon energy E' and the scattering angle θ can be derived as

$$hv' = \frac{hv}{1 + \frac{hv}{m_0 c^2}(1 - cos\theta)} \tag{2}$$

where m_0 is the electron mass and c the speed of light [13]. A head-on collision in which $\theta = \pi$ has the maximum energy that can be transferred to an electron in a single Compton interaction, and thus marks the Compton edge. All scattering angles below π creates the Compton Continuum, also called the Compton shelf. The lower peak, called the backscatter-peak, arises when gamma-photons hits the shield around the detector, and Compton scatters back in the detector with reduced energy.

The main full-energy peak, or in some radioactive sources multiple peaks, arises when the full gamma ray energy is deposited in the detector. The most likely interaction for depositing all its energy is photoelectric absorption. In a Compton scattering event the scattered photon may be absorbed, and the added energy of both instances are equal to the total energy. These pulses have a well defined average height, but there will be some statistical variation arising from the discrete nature of the measured signal, which creates a small deviation. However, these variations are small, so any measurements done by a detector will be indicative of its own limited resolution. [3]

Photoelectric absorption is the most dominant interaction when the gamma ray energy is below 200keV. Compton scattering dominates from 300keV to several MeV, which is the gamma ray imaging energy range of the CdZnTe detector. The third type of interaction is pair production, where the electron is replaced by an electron-positron pair. However, Pair production is predominantly confined to high energy gamma rays (above 1.02MeV).

2.2 Weighting Potential

CdZnTe is a room-temperature semiconductor material for radiation detectors that is highly suited for high resolution gamma ray spectroscopy due to its good electron

transport properties and commercial availability [5]. When a gamma ray interacts with a semiconductor detector through one of the three processes discussed earlier, electrons or electron-positron pairs are created. The energy of the particle is lost by ionizing the detector material, which creates a number of electron-hole pairs proportional to the energy loss of the gamma ray within the detector. The applied electric field across the semiconductor detector drives the electrons and holes towards the anode and cathode, respectively. The movement of these charge carriers introduce a signal on one or more of the electrodes. The induced charge ΔQ is proportional to the number of electron-hole pairs, and is consequently heavily dependent on the movement of the charge carriers. The Shockley-Ramo theorem is a simplification of the calculation of the induced signal, and is the basis behind the development of modern CdZnTe detectors[4]. The theorem states: the charge Q on an electrode induced by a movement of a point charge q is given by

$$Q = -q\psi_0 \tag{3}$$

where ψ_0 is the weighting potential. It follows that the change in induced charge is given by

$$\Delta Q = -q\Delta\psi_0 \tag{4}$$

ΔQ is converted to a voltage pulse that can be measured as a pulse height, and by counting the instances of these pulse-heights, an energy spectrum from the respective sources may be constructed, as explained in the introduction of this section. The true electric potential is determined by the actual operating electric field and the space charge density, but the weighting potential is a virtual potential used as a tool in order to do a more simplistic calculation of the induced charge ΔQ. For a pixelated detector, the weighting potential for the cathode and collecting anode pixel are as shown in figure 4, illustrating the linear depth dependencies of the cathode and weak depth dependencies of the anode signal[11].

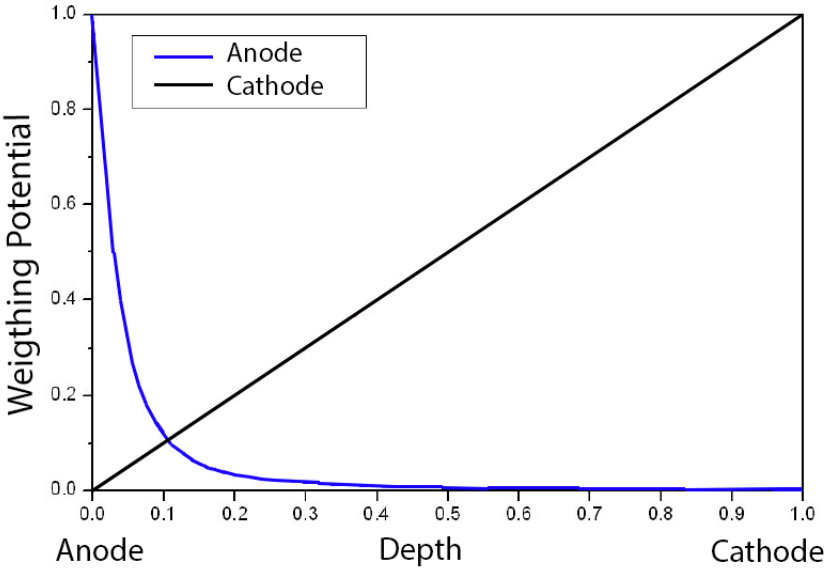

Figure 4 – Calculated weighting potential of an anode pixel(blue) and the cathode(black) as a function of depth[7].

2.3 Single and Multiple Interaction Events

Compton scattering can, as explained in figure 2.1, cause several interaction within the detector crystal as illustrated in figure 5. Each interaction will induce charge on separate pixels, and thus register as two separate events. The induced charge in each pixel must be added to find the true amount of deposited charge from the gamma ray.

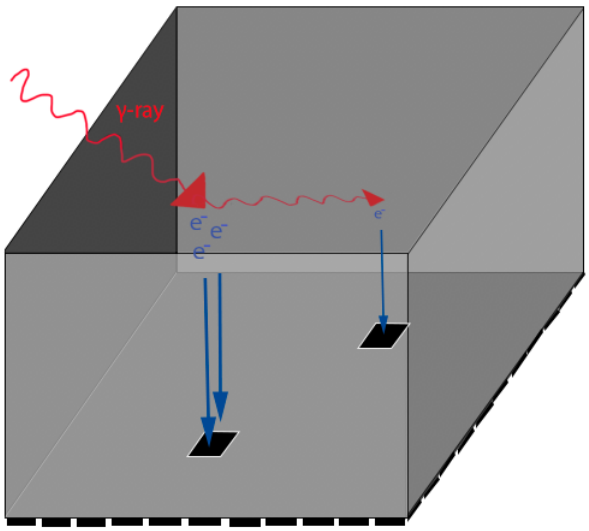

Figure 5 – Simple illustration of a multiple interaction event: A Compton scattering event. The red arrow represents a gamma ray, the blue lines represent the resulting electrons after an interaction with the crystal, and the black square represents the induced pixel anode.

If there is only one interaction, as in a single photoelectric absorption or a scattering event, where the scattered ray escapes the detector, only one pixel receive charge as depicted in figure 6. This will categories as a single interaction event.

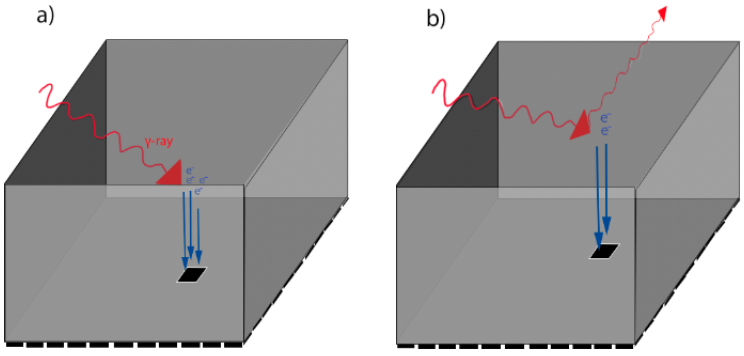

Figure 6 – Schematic illustration of two examples of single interaction events. a) illustrates a complete photoelectric absorption. b) illustrates a scattering event where the scattered ray escapes the detector. The red arrow represents a gamma ray, the blue lines represent the resulting electrons after an interaction with the crystal, and the black square represents the induced pixel anode.

There are, however, mechanisms that can cause a single interaction event to appear in multiple pixels. Electrons inducing charge in one pixel have a chance of momentar-

ily travel through a higher neighboring-pixel weighting potential, inducing transitory charge on the neighboring pixel. The transient charge could be interpreted as an interaction, if large enough. This phenomenon is known as weighting-potential crosstalk and could cause a degradation in the resolution. Since the radiation interaction creates a charge cloud, there is a chance that some charge will end up in neighboring pixels. Especially when the charge cloud is large or is created directly above the gap between two pixels. This phenomenon is called charge-sharing[**?**]. As the charge cloud stems from a single interaction, the two events should be treated as such and be added together. However, it is hard to distinguish a charge sharing event from side-neighbor Compton scattering. Efforts have been made to distinguish between such events, concluding that the most effective strategy is to treat all side-neighbor events as charge-sharing events and combine them into a single interaction[14].

2.4 C/A Ratio

In semiconductors such as CdZnTe there is a chance of charge-trapping from any impurity or lattice defect[6]. The longer an electron needs to travel, the higher the chance of electron trapping, which lead to fewer electrons to be collected by the anode. However weighting potential as depicted in figure 4 results in larger signal from interactions near the cathode as the weighting potential is larger. These depth dependence will result in a poorer resolution if not corrected for. Given these depth dependencies, the signals induced on the cathode and collecting pixel from an event can be approximated as [7]

$$S_c = ne(1 - z) \tag{5}$$

$$S_a = ne \tag{6}$$

where n is the number of electrons created and $(1 - z)$ is the depth of interaction. Thus, the interaction depth can be calculated from the ratio between the cathode and anode signals as

$$R = (1 - z) = \frac{S_c}{S_a} \tag{7}$$

This signifies that a method of approximating the depth of an interaction is using the ratio of the cathode signal to the anode signal, known as the C/A ratio[8].

By dividing the spectrum into sub spectra dependent on interaction depth gain factors for each depth interval can be calculated by measuring the photo peak centroid of each sub spectrum and find the relative coefficient to a desired peak. The gain factors are then used to align all photo peaks, as illustrated in figure 7. Depth correction based on C/A ratio is limited to single interaction events, i.e only one collecting anode. For multiple interaction events, the cathode amplitude will consist of a sum of several interactions and can not be used to calculate the ratio [7].

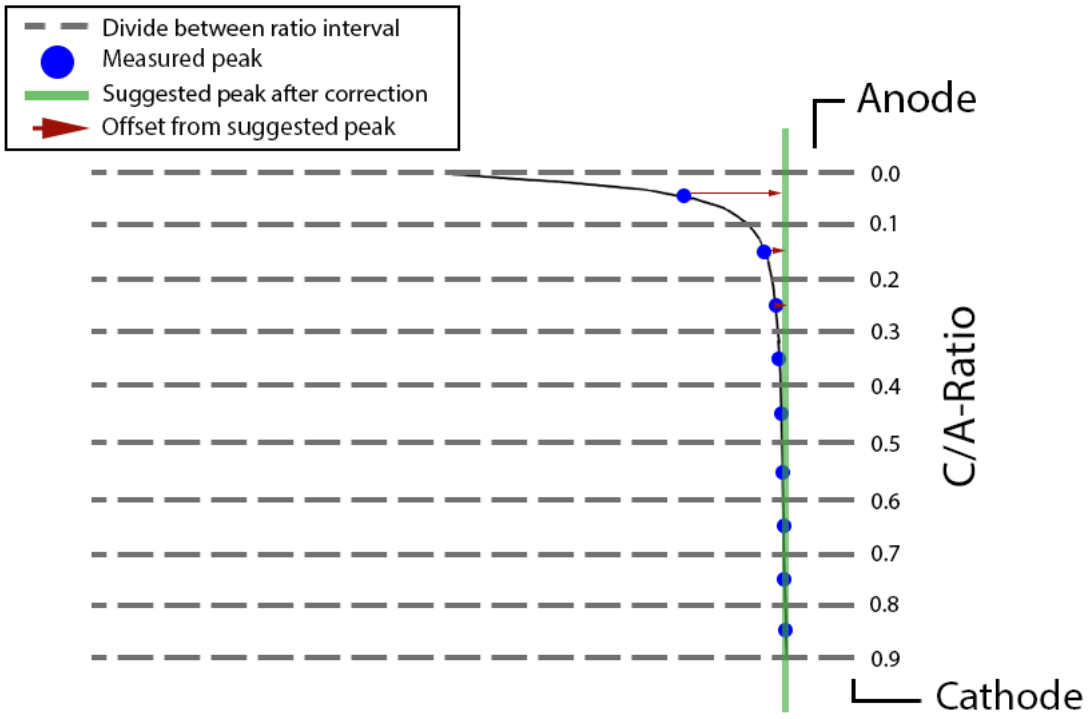

Figure 7 – Illustration of how the depth of interaction affect the spectrum when divided into sub spectra and how C/A-ratio can be used to correct the offsets.

2.5 Pulse Height Analysis

To achieve a high resolution spectrum, it is crucial to estimate the signal amplitude for each event with high accuracy, and to differentiate between good pulses and noise that could degrade the energy resolution. The theory behind the two methods for pulse height analysis is explained in this section.

2.5.1 Trapezoidal Filter

The trapezoidal filter is a traditional filter used to determine the signal amplitude. A digital trapezoidal filter uses two moving average filters of length L, where one filter is shifted by G points. The output is produced by the ith value of the first window subtracted by the ith value of the second window as shown in equation (8) [16]

$$\begin{aligned} V_{\text{win1}}[i] &= \frac{1}{L}\sum_{j=0}^{L-1} V[i+j] \\ V_{\text{win2}[i]} &= \frac{1}{L}\sum_{j=0}^{L-1} V[L+G+i+j] \\ V_{\text{out}} &= V_{\text{win2}} - V_{\text{win1}} \end{aligned} \tag{8}$$

where $V[i]$ is the input signal amplitude. When the filter is applied, the output pulse becomes trapezoidal with peaking time Δt_{L} and shaping time equal Δt_{G}, as depicted in figure 8. The values Δt_{L} and Δt_{G} are based on the filter lengths L and G and system sample rate. The height of the trapezoidal corresponds to the amplitude of

the input pulse, which in turn means it is proportional to the energy deposited by the particle in the detector.

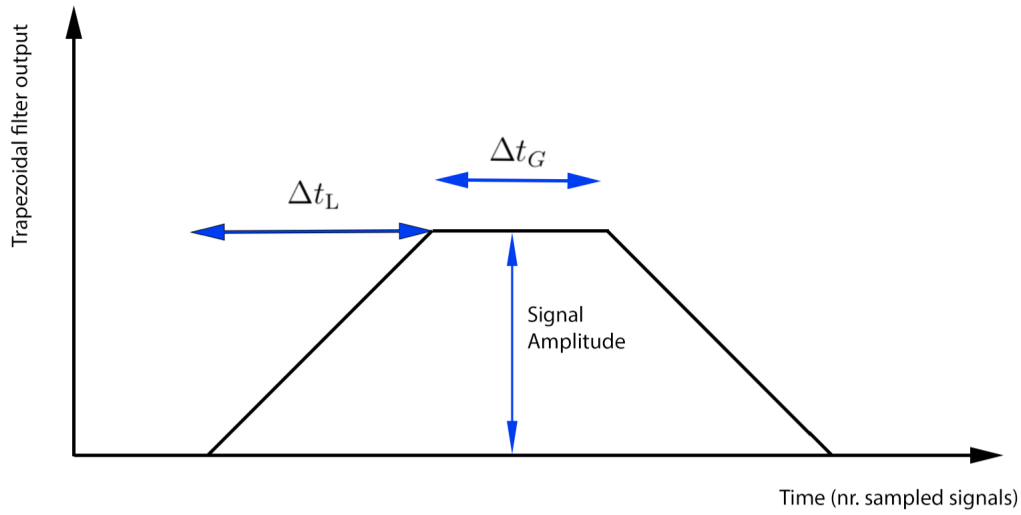

Figure 8 – A simple illustration of a trapezoidal output. Δt_L is the peaking time and Δt_G the shaping time.

2.5.2 Gaussian Mixture Model

The second method for pulse height analysis is based on Gaussian Mixture Model (GMM). The GMM is a probabilistic model for representing sub populations from an overall population as a multiple of normal distributions. The one-dimensional model is given by

$$p(x) = \sum_{i=1}^{K} \pi_i \mathcal{N}(x|\mu_i, \sigma_i) \quad \text{where} \quad \mathcal{N}(x|\mu_i, \sigma_i) = \frac{1}{\sigma\sqrt{2\pi}} \exp\left(- \frac{(x-\mu_i)^2}{2\sigma_i^2} \right) \tag{9}$$

where μ_i is the mean and σ_i is the variance. The multi-dimensional model with K elements is given by

$$\begin{aligned} p(x) &= \sum_{i=1}^{K} \theta_i \mathcal{N}(x|\mu_i, \sigma_i) \quad \text{where} \\ \mathcal{N}(x|\mu_i, \Sigma_i) &= \frac{1}{\sqrt{(2\pi)^K \mid \Sigma_i \mid}} \exp\left(- \frac{1}{2}(x-\mu_i)^T \Sigma_i^{-1} (x-\mu_i) \right) \end{aligned} \tag{10}$$

where μ_i is the mean and Σ_i is the covariance matrix. Each data point has a probability of being generated by each of the distributions. The model's parameters are estimated by the Expectation-Maximization(EM) algorithm: Given some statistical model which generates a set of observed data X, some latent data Z, and a vector of unknown parameters Θ along with a likelihood function $p(X, Z|\Theta)$, the maximum likelihood

estimate (MLE) of the unknown data is found by maximizing the marginal likelihood of the observed data. This is done by iteratively applying the two following steps until convergence. The estimation step

$$Q(\Theta|\Theta^{(t)}) = E_{Z|X,\Theta^{(t)}}[\log p(X, Z|\Theta)] \tag{11}$$

where $Q(\Theta|\Theta^{(t)})$ is defined as the expectation value of the log likelihood function of Θ, with respect to the current conditional distribution of Z given X and the current estimates of the parameters $\Theta^{(t)}$. And a maximization step

$$\Theta^{t+1} =_{\Theta} Q(\Theta|\Theta^{(t)}) \tag{12}$$

which maximizes the expected value [17]. In other words, the EM algorithm is an iterative process that assumes random components (randomly centered on data points usually learned from *kmeans* [20]) and computes weights encoding a probability of each point being generated by each component in the model. Then, given those assignments, it maximizes the likelihood of the data.

2.6 Energy Resolution

A way of examining the quality of data is to examine the distribution of the full-energy peak of a radioactive source. Figure 9 illustrate a comparison of data with poor resolution and good resolution.

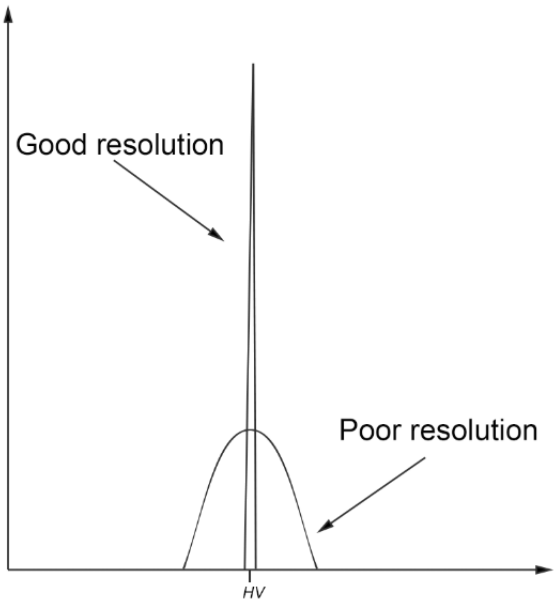

Figure 9 – Examples of full-energy peaks comparing detector energy resolution with good resolution and poor resolution

The formal definition of detector energy resolution is given as

$$R = \frac{FWHM}{H_0} \tag{13}$$

where H_0 is the position of the peak centroid and FWHM is the full width at half maximum [9]. The definition assumes any background or continuum that the peak might be superimposed on is subtracted. When FWHM is used in this thesis, it means the entire definition of R.

3 Previous Work

Development of CdZnTe-detctors have been on-going since the 1990s and great efforts have been done to achieve a high spectral resolution and reach the theoretical resolution of 0.2% FWHM at 662keV [3]. CZT has been registered to achieve a resolution as low as 0.48% FWHM at 662keV[19].

Earlier work, using a predecessor of the IDE3421 ASIC, has achieved a spectral resolution below 1% FWHM at 662keV for single pixel events with a 15mm Redlen CZT detector. In order to achieve this result, several traditional filters such as Triangle, CR-RC, and Gaussian filters were tested, with the trapezoid filter found to have the best performance among the traditional filters for charge-collecting pixels. For transient signals, CR-RC was proven best. To achieve the below 1% spectral resolution, correction of depth interaction was introduced using C/A ratio. Multiple interaction correction using drift time was attempted and resulted in an FWHM above 1%. The broader peak was said to be caused by noise introduced by the cathode, as it has large electrode capacitance and leakage current. [18]

This thesis is a continuation of a specialization project which worked with the IDE3421 ASIC in a single module system. A calibrating routine was proposed, consisting of characterizing and correcting variations in baseline levels and gain. A new technique for pulse height analysis using Gaussian Mixture Models was proposed and compared to the traditional trapezoidal filter. The trapezoid filter method achieved energy resolution of 2.56% FWHM at 662keV for ^{137}Cs and the GMM method achieved 2.72% FWHM at 662keV.[1]

4 System Description

4.1 Overview

The system to be calibrated is the GDS-100, created by IDEAS. The description provided is an outline of the realized system where only the most essential components are included. A diagram of the main parts is depicted in figure 10 .

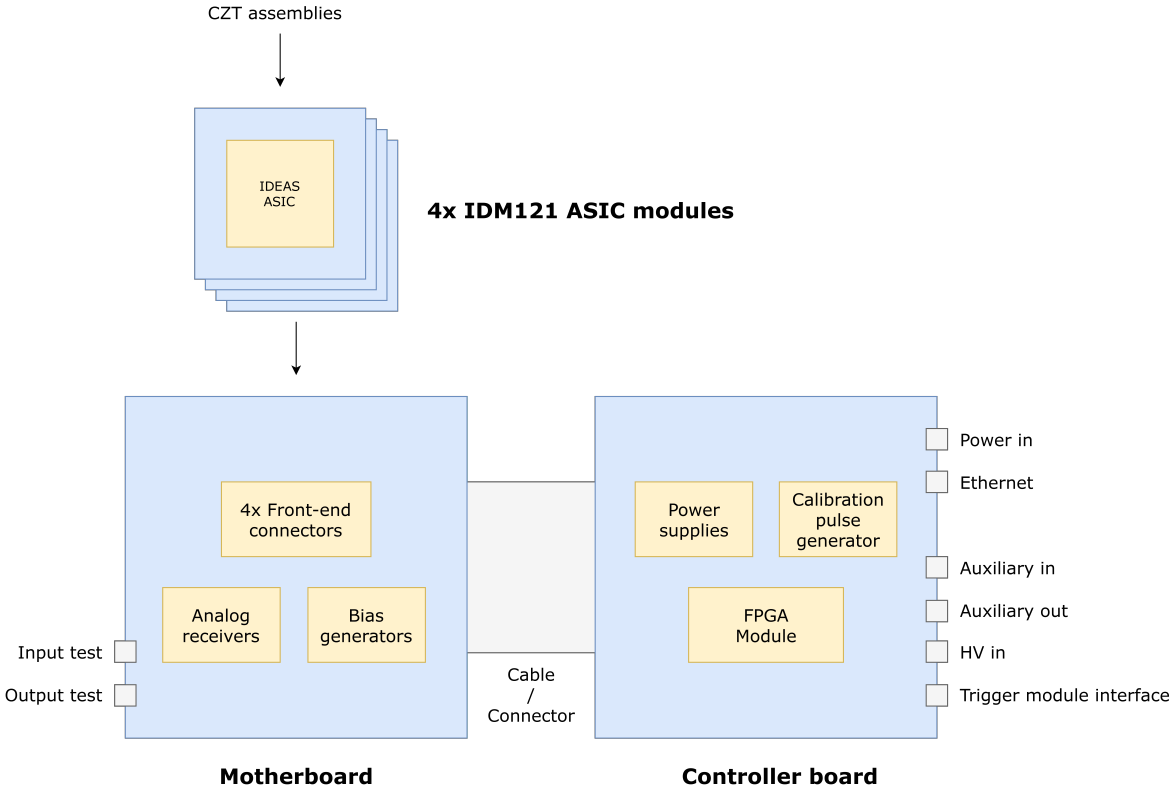

Figure 10 – Diagram of the GDS-100 system.

The system consists mainly of a motherboard and a controller board. Four ASIC modules can be fitted on the motherboard, where each ASIC holds a CZT-crystal. The motherboard handles analog signals transmitted from any of the four ASIC modules and digitizes them for further transmission to the controller board. The controller board is powered by a single 6V supply and distributes the power to all parts of the GDS-100 system. Another central function covered by the controller board is an internal calibration pulse that generates square pulses with adjustable amplitudes, used to read front-ends without any detector attached. In addition, the board includes a high voltage used to provide bias for the CZT detectors. An illustration of the GDS-100 system is depicted in figure 11.

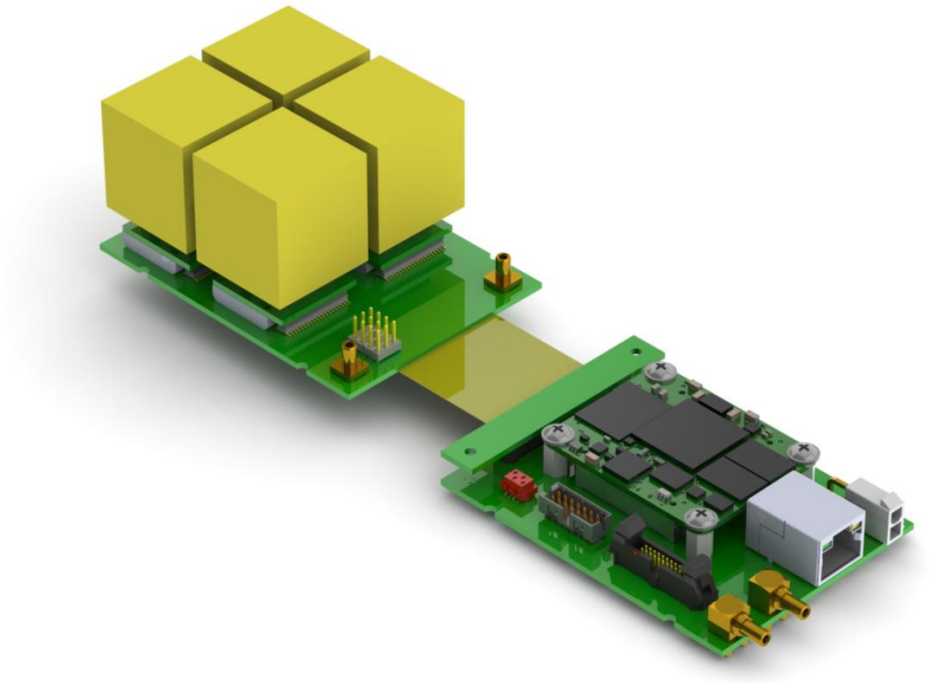

Figure 11 – Illustration of the GDS-100 system.

The ASIC modules are IDE3421, designed for use with CZT radiation detectors. The detector is connected to a bias voltage and has cathode and anode outputs. The anode of the detector is divided into an 11x11 pixelgrid with pixel size 1.22mm x 1.22mm. The ASIC contains 128 pre-amplifier inputs for the negative charge from each of the anode pixels and additional inputs for the positive charge from the CZT cathode. Figure 12 shows an illustration of a CZT detector with one ASIC input.

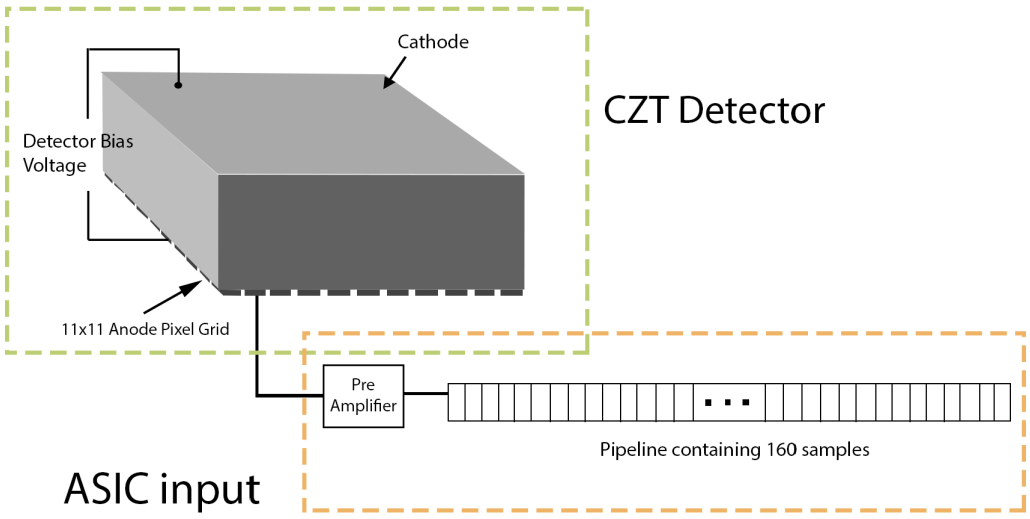

Figure 12 – A simplified illustration of an ASIC module. The CZT-detector with corresponding features: Detector bias voltage, cathode and anode pixelgrid are outlined in green. One ASIC input with pre-amplifier and 160-cell pipeline is outlined in orange.

Each pre-amplifier output is continuously sampled, and the values are stored in an

analog ring buffer (160-cell pipeline). This provides a snapshot of the voltage-levels before and after an gamma radiation event hits. The energy amplitude can be derived from the voltage difference as illustrated in figure13.

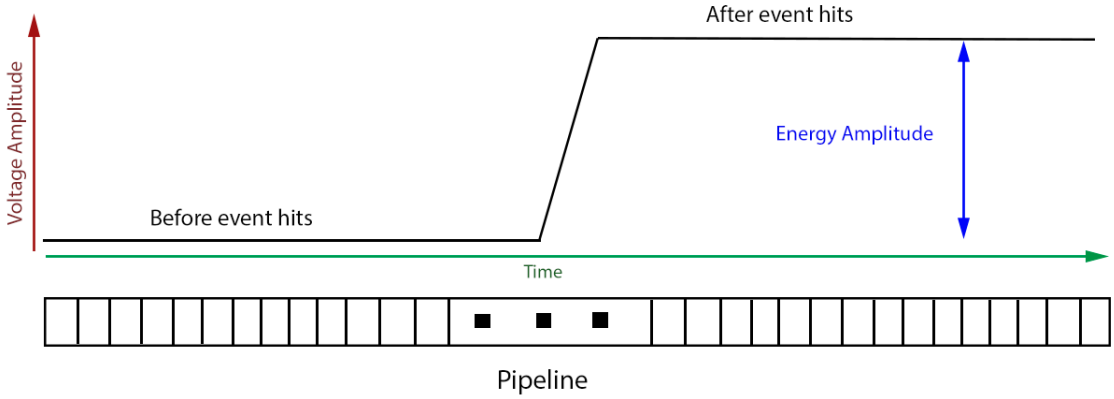

Figure 13 – An illustration of how the samples in the 160-cell pipeline are translated into an energy amplitude.

The pipeline samples are digitized by an external ADC and are collected with a header in an external FPGA. Full header description is provided in Appendix A. The datapackets are sent via Ethernet and written directly to a file on a host computer. The system calibration settings are set through a customized test-bench created by IDEAS. Some important system features are presented in the table 1.

Table 1 – System Settings

Parameter	Typical	Description
Threshold, VTHR	AVREF -50mV = 1750	Voltage on a the level discriminator that determines which signal amplitude will cause a trigger.
High Voltage, detector bias HV	-2500V	The voltage applied to the cathode side of the CZT detector.
Clk Frequency	50Mhz	System clock. Pipeline sampling speed.
Readout frequency	6.25MHz	A/D converter sampling speed.
Read mode		(1)Triggered channels with 4 neighbors. (2)Triggered channels with 8 neighbors. (3)All channels.
SH-DELAY	80	Determines the number of samples after the trigger.
Trans-Impedance Amplifier Gain (TIA)	100[mV/mA]	The ASIC output signal is a current that is proportional to the charge from the preamp at the point of sampling in the order [μA/fC]. This has to be converted to voltage before the A/D converter.
Trigger Type		The ASIC has two readout modes: (1) System auto forced readout mode, which is triggered by the system clock. (2) Non-forced readout mode, which is triggered by a physical event. (Gamma-ray or noise)

4.2 System Error Adjustments and Corrections

4.2.1 Readout Chain Description

While the system at hand is considerably more complex, it is based on the traditional analog chain presented as a block diagram in figure 14.[15]

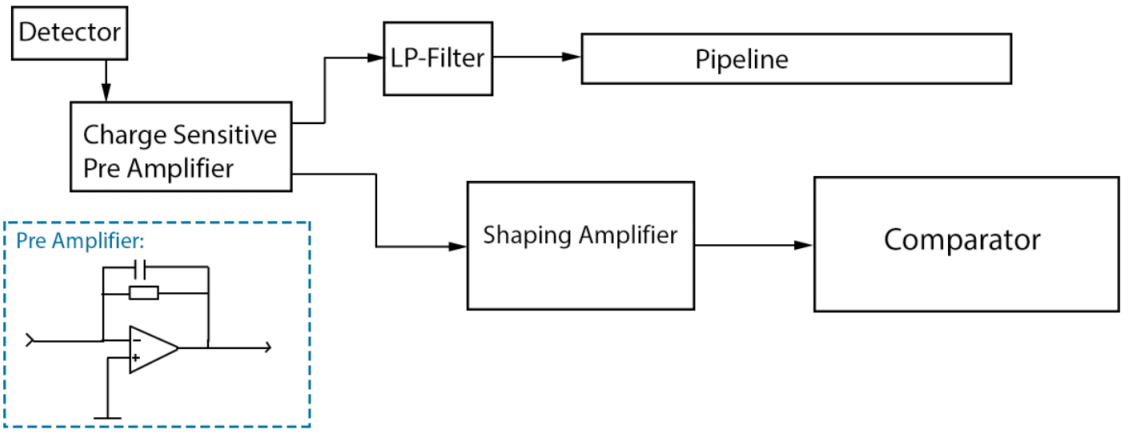

Figure 14 – Blockdiagram of the analog chain of which the GDS-100 is based on. The charge-sensitive pre-amplifier receives the signal generated in the detector and converts it to a voltage amplitude. The signal is then sent through a lowpass filter and sampled in a pipeline. The pre amplifier output is also sent through a shaping filter to a comparator which check if the amplitude is above a programmable threshold.

The first stage is a charge-sensitive pre-amplifier that receives the signal generated in the detector. The pre-amplifier integrates the signal from the detector and converts it into a voltage amplitude. The feedback capacitor determines the gain that translates to the magnitude of the pre-amplifier output voltage for a given input charge. In an ideal situation the pre-amplifier is simply made of a capacitor. However, to avoid saturation there is a discharging resistor in parallel that results in a signal with a fast rise-time that returns to baseline within a time determined by a programmable resistance. If the resistance is too low, there is a higher chance of noise being integrated, creating a noisy signal. On the other hand, if the resistance is too high, the signal will return to baseline too fast and the true amplitude will not be recorded. This is illustrated in figure 15.

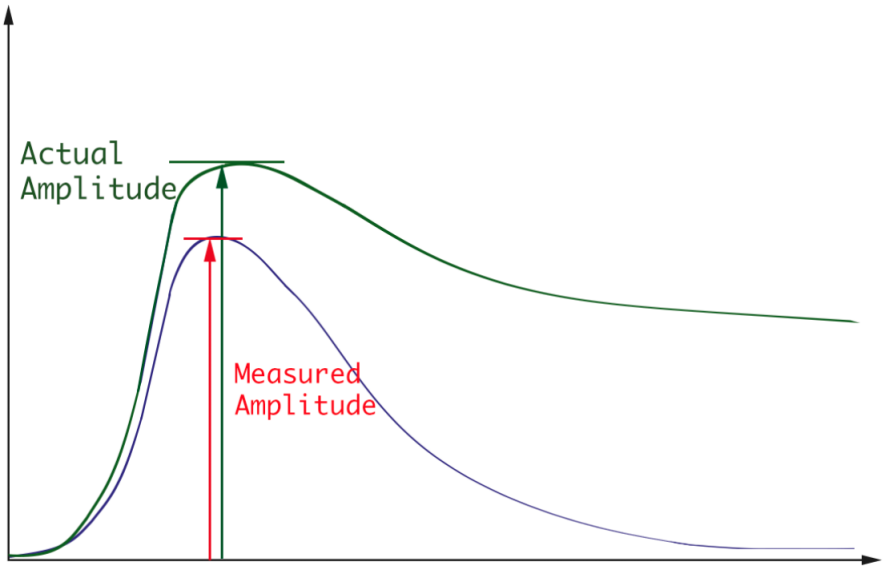

Figure 15 – Illustration of potential amplitude difference if the feedback resistor in the pre-amplifier is too large.

The pre-amplifiers output go through a Low-Pass filter to avoid anti-aliasing and is sampled at a programmable sampling frequency. The corresponding charges are stored in capacitors, i.e. the pipeline. Process variations in these capacitors will change their value slightly, which translates to signal variations that need to be corrected for.

As depicted in Figure 14, the pre-amplifier output is also connected to a shaping amplifier, and further to a comparator that generates a trigger if the input charge exceeds a programmable threshold. If the threshold is too high, then low-energy events will not trigger. A fraction of the energy of an event could leak into a neighboring pixel, resulting in lower signals. If not added back into the event, the true energy will not be registered. However, if the threshold is too low, high noise-peaks might give false triggers. A constant flow of noise triggers can overpower the system, which will be busy reading out noise instead of triggering on true events. Both situations are illustrated in figure 16. The system can force a readout of all neighboring pixels, which allows for higher threshold without losing low-energy events.

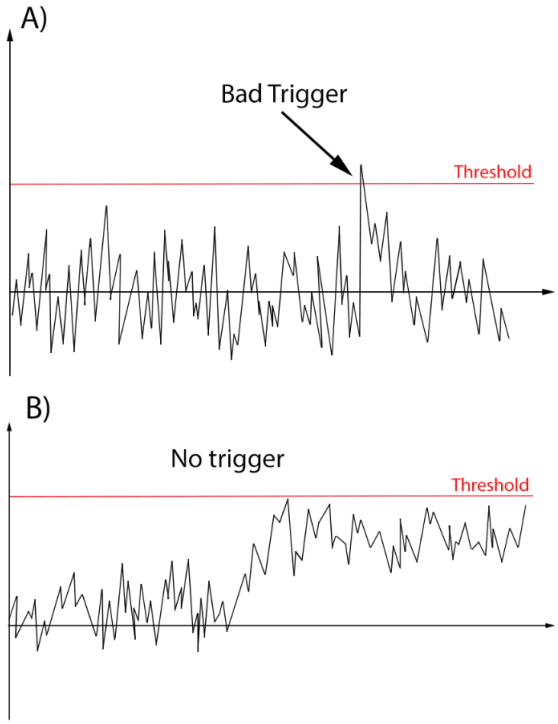

Figure 16 – A) Illustration of a bad trigger caused by a noise peak reaching the threshold(red). B) Illustration of a low energy event not causing a trigger

The channel design is copied for each channel, and should, in theory, be identical. However due to process-variations there will be small changes between each channel, causing offsets,i.e different pedestals, and gain-variations in the measured values. The feedback resistances of both pre-amplifiers and shaping amplifiers are created by transistors in order to save space and have more configuration-options, which all have slight variations in linearity. Adding to these effects, the physical placement of each channel will give temperature differences between channels. The pre-amplifiers and shapers also need bias voltage, which is generated internally. The distance from the bias generator give voltage-level variations that may result in power drop from resistance within the wire. All of these effects contribute to gain variations and offsets.

4.2.2 Corrections

Pedestal Correction As each cell will have a different baseline from variations in hardware characteristics, a pedestal correction is done. The pedestals can be calibrated by a readout of all cells without a signal being present on their pre-amplifier. The procedure of obtaining the pedestals is simple and consists of two steps:

1. Using an internal readout mode, acquire a dataset with a certain number of events for all channels.

2. Take the average of each cell's amplitude for all channels.

There is some cross talk between the hold signal and pre-amplified signal that has to be taken into account, as it will create interference in the start-cell. There are two readout modes as listed in Table 1. In forced readout mode, the readout start-cell is specified and is the same for each event. The error is avoided by doing a readout

with a sufficient amount of events sampled with a few different specified start-cells. In non-forced mode the readout start cell is defined by where the continuously sampled channels are triggered, so the error is avoided. Figure 17 shows an example of an event before and after pedestal correction.

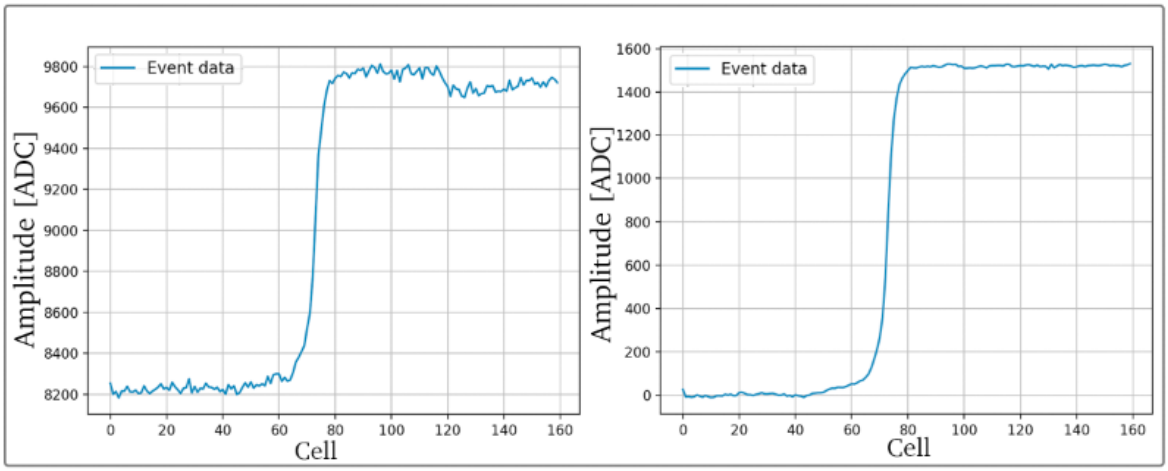

Figure 17 – Example of event before(left) and after(right) pedestal correction

Noise The system noise in each channel can be used to uncover channels that introduce a large amount of noise into the system which can skew the results. Noise can be measured by the standard deviation of all baseline measurements. Another noise measurement is input referred noise, calculated by sending the baseline measurements through a pulse-height filter and calculate the standard deviation of the resulting pulse-heights.

ADC Differential Non-linearity ADC creates bias towards the frequency it uses certain numbers within the ADC bins, so called non differential linearity. In order to minimize these effects, a random number between -0.5 and 0.5 is added to the original data before pedestal subtraction in order to smear the data.

Linearity and Gain Variations Figure 18 represents the ideal linearity relationship between the input charge and output voltage, however due to the variation discussed in this chapter there will be non-linearity. The magnitude of linearity can be found by measuring the output voltage with incremental magnitude of input charge and find the deviation of each sample from a linear fitting.

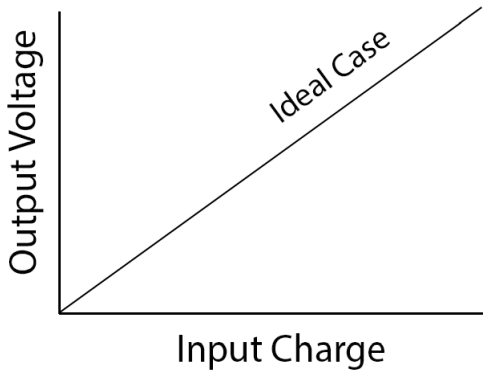

Figure 18 – Illustration of the ideal linear relationship between input charge and output voltage.

The gain between input charge and output voltage may vary between channels, as explained earlier in this section. Large variations in gain will result in a broader peak, thus need to be corrected for. Gain correction are done by finding a gain factor for each channel that can be multiplied to all events within the respective channel.

Two methods suggested to find these gain-factors are 1) Using the internal calibration pulse to send a large amount of pulses of incremental magnitude to each channel, and do a linear fitting on the average value of each increment. 2) Take data from known sources and create an energy spectrum for each channel. The gain factor is then calculated by comparing ADC values of the measured peaks to the known energy values of the radioactive sources used.

The first method automatically converts the new value into keV. The second method only aligns peaks, however the calibration pulse is connected to a 1pf capacitor, and by measuring the output from the calibration pulse, resulting charge can be estimated from[10].

$$Q = C * V = 1pF * V_{measured} \tag{14}$$

5 User Interface

5.1 GDS-100 Calibration User Interface

This chapter will give an introduction to the *GDS-100 calibration user interface* and all its features. The intention of the *GDS-100 calibration user interface* is to provide an example of a calibration routine to give insight of the necessary steps when translating the raw binary-file that the system provides into a high resolution energy spectrum. The software is also meant to be used as an analytical tool to investigate any limitations of the system and discover possible causes of error within the readout sequence.

The software is written in *Python 3.7* using the *PyQt5* framework[23] and supports iOS and *Windows* with slight design-differences. Multithreading allows the interface to simultaneously function as a processing script, implemented with *Python* library *threading* [21]. A customized software created by IDEAS is the *Testbench*, which are provided with the GDS-100 system. System settings are set trough this software and it processes the detector readout data into a raw binary-file. The IDEAS *Testbench* has a built in compilator that only supports Python 2.6 and limited additional libraries. Hence, the calibration user interface has been created as an add-on solution to work in tandem with the *Testbench* and some additional *Testbench* scripts to create a full readout and calibration routine. The *Testbench* only supports *Windows*.

The procedure that the *GDS Calibration User Interface* present is divided into two steps. First step is to calibrate the system, and the second is to process and visualize source data. Both steps will be presented and described in the following sections. Each step works with data provided in a binary format, and in order to process it, the data is sorted into DataFrames[2], using the *Panda* library[22]. Each row includes timestamp, channel-type, channel coordinates within the pixelmap, ASIC number, trigger-cell and cell data of all 160 cells. The source code of the user interface can be found at `https://github.com/sofiago/Master-2021.git`.

5.2 Start Page

The start page is presented in figure 19. The initial page presents two options: to either calibrate the system or go directly to process source data. The interface needs new calibrating data for every new setup, but after calibrating once, the user can go directly to process data even if the software has been exited and restarted. There is also the design option of dark mode and light mode to satisfy the user preference.

[2]two-dimensional labeled data structures with columns of potentially different types

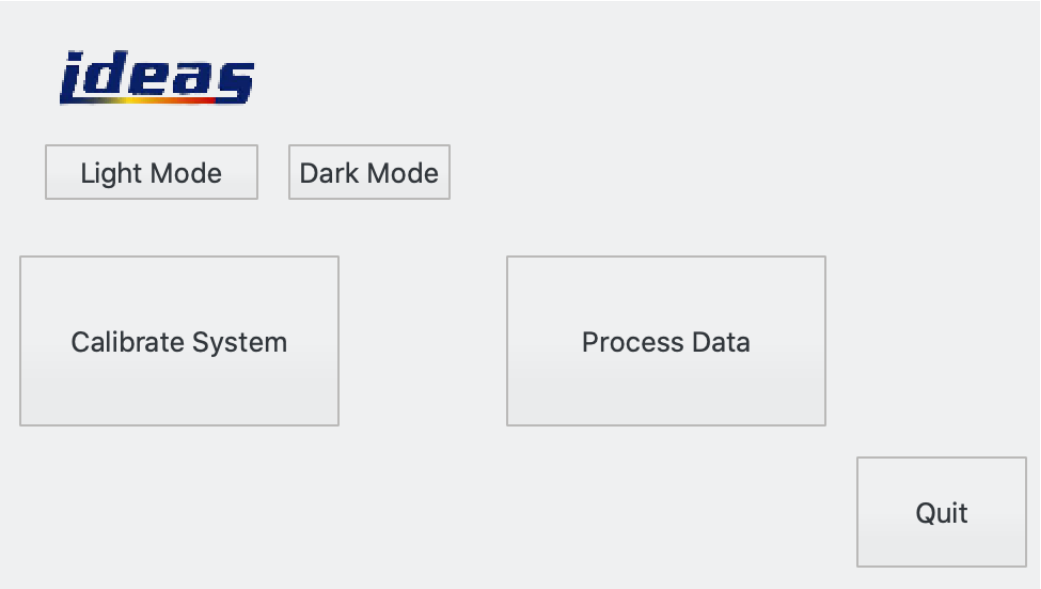

Figure 19 – Start page of the *GDS-100 calibration interface.*

5.3 Step 1: Calibrate system

Step one is to calibrate the system. The main goal is to calculate the values for offsets and gain variations as explained in 4.2.2. Each of the four possible ASICs has one tab, as depicted in figure 20.

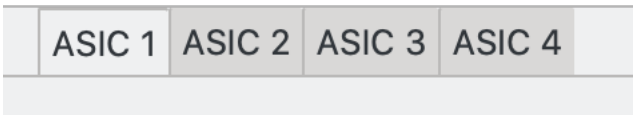

Figure 20 – Tabs to select ASIC module.

The overall calibration interface layout is depicted in figure 21. It mainly consists of three different pixelmaps with corresponding distribution-plots. Each pixel represents one channel, and the layout follows the physical placement of that channel within the ASIC.

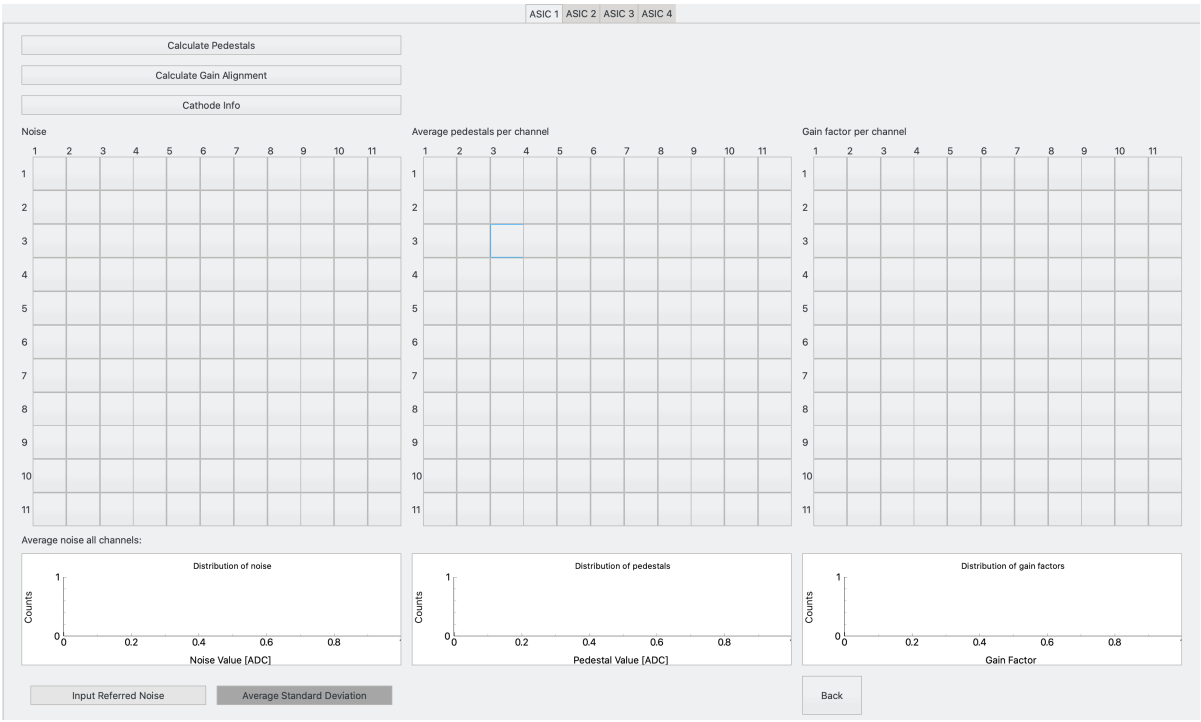

Figure 21 – Initial layout of calibration interface.

Each pixelmap provides information in one of the following areas:

- Noise (standard deviation and input referred noise)
- Pedestals
- Gain

Noise The pixelmap dedicated to noise readout can either show input referred noise or standard deviation as explained in 4.2.2, changed simply by clicking the corresponding button to the bottom left as depicted in figure 22.

Figure 22 – Buttons to either select to display input referred noise or average standard deviation.

An example of the noise pixelmap and corresponding distribution with example data is depicted in figure 23. The pixelmap works as a heatmap which allows the user to clearly recognize channels with high noise contribution.

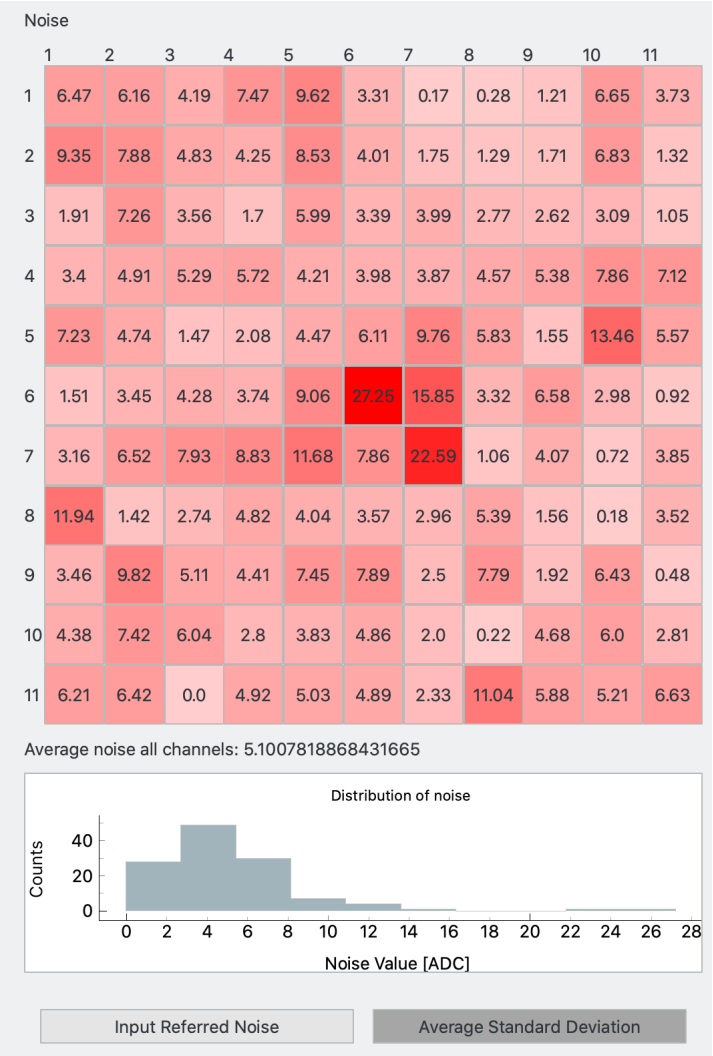

Figure 23 – An example of the noise pixelmap displaying average standard deviation. Each pixel displays the amount of noise within the corresponding channel.

Pedestals The *Testbench* must provide a data-file containing a specified number of baseline readouts using the internal readout mode which forces a readout of all channels. The readout script within the *Testbench* uses a custom library to set system-settings. The data is stored in a specified path that the calibration interfaces can retrieve. The full readout script is provided in appendix C. Figure 24 depicts an example of pedestal data.

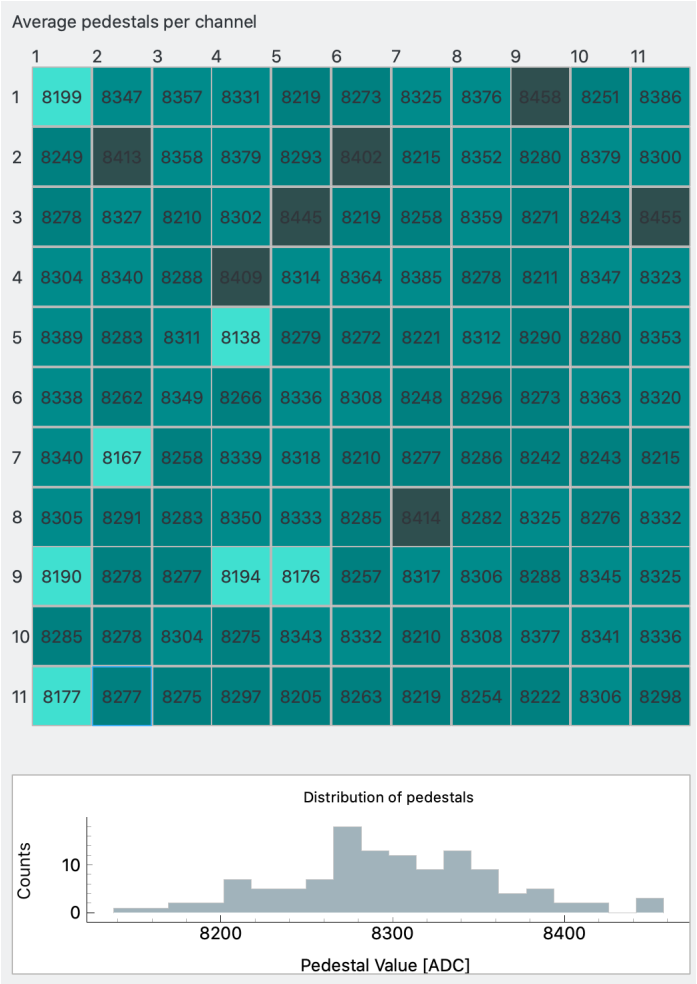

Figure 24 – An example of the pedestal pixelmap. Each pixel displays the average pedestal of the corresponding channel.

Gain The gain-factor is calculated using the internal calibrating pulse. The *Testbench* must generate a data-file containing readouts of a specified number of pulses with a specified amplitude to each channel, with all other channels deactivated. The data is stored in a specified path that the calibration interfaces can retrieve. The full script is provided in appendix C. An example of gain data is depicted in figure 25.

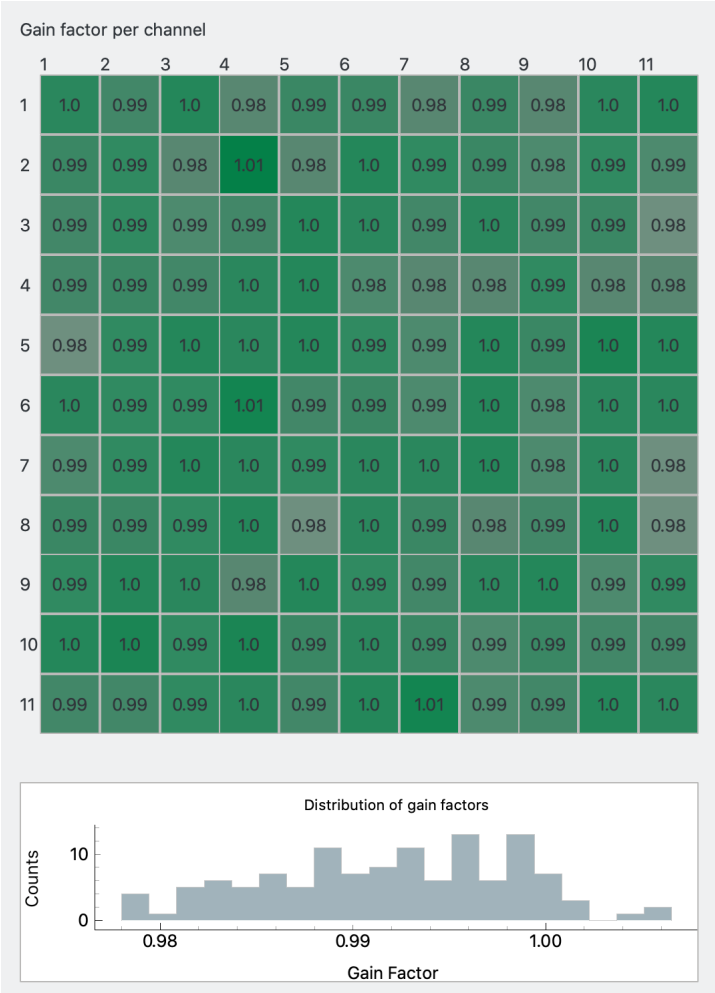

Figure 25 – An example of the gain factor pixelmap. Each pixel displays the calculated gain factor of the corresponding channel.

Additional information Each pixel in either pixelmap displays an additional pop-up window when pressed. An example of a pixel window is depicted in figure 26. The window display more in depth information about the corresponding pixel.

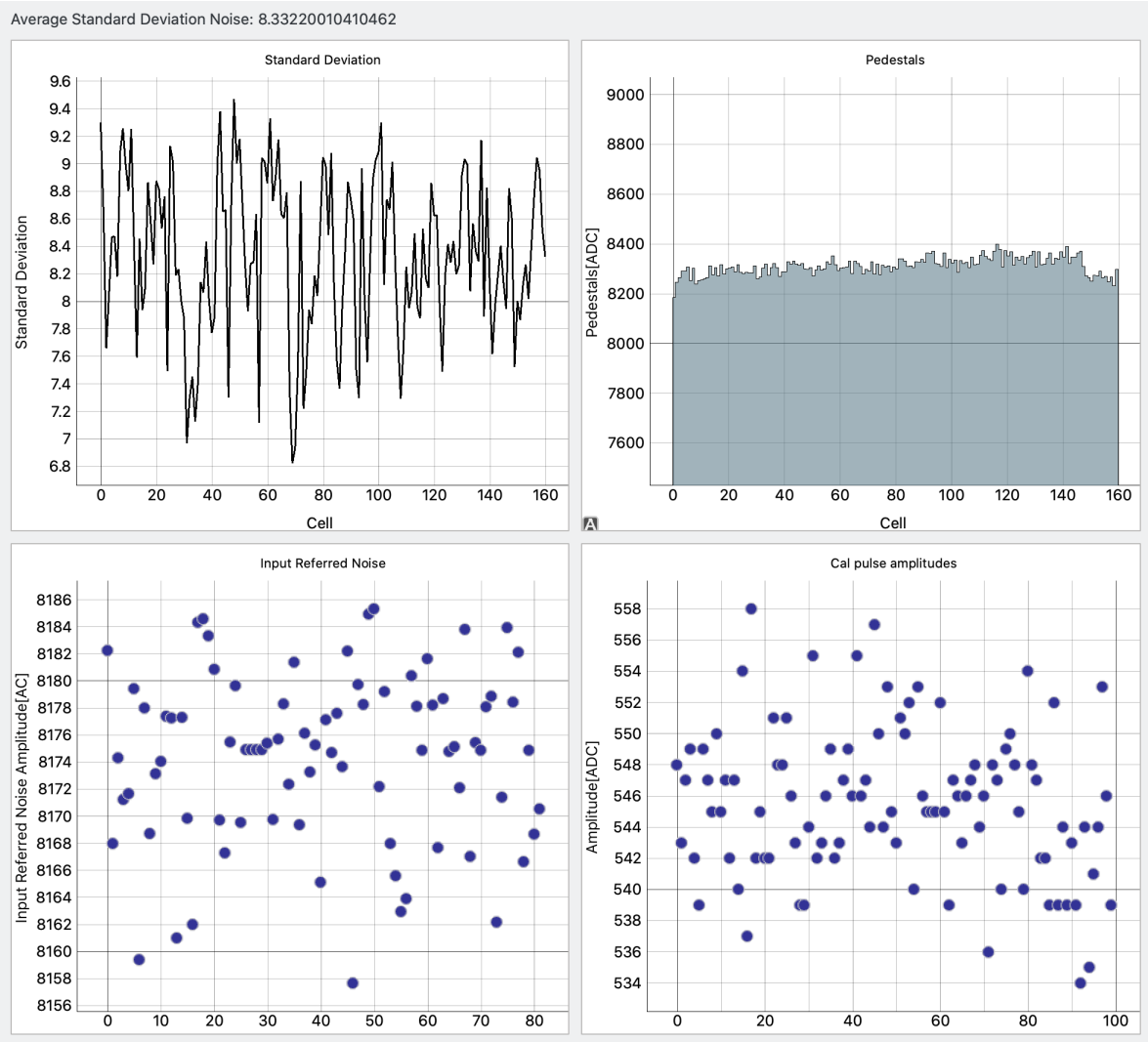

Figure 26 – An example of the calibrated channel #39. Top left graph displays the standard deviation for each cell. Bottom left graph displays all instances of recorded input referred noise, top right graph displays pedestals for each cell and bottom right displays all instances if recorded calibration pulse-heights.

The top two graphs display the standard deviation and offset values of each graph. Bottom left graph depicts the recorded instances of input referred noise, and bottom right displays all instances if recorded calibration pulse-heights. The bottom two graphs are mainly visualized to inspect the quality of the calibration-data. Large outliers may suggest that the readout was compromised by example, cosmic background noise or an error within the readout-sequence.

Cathode The button with label *Cathode Info* offer a layout with the same information as the anode channels. The gain graph is excluded as the cathode gain is not comparable with the anode gains. The cathode layout is depicted in figure 27.

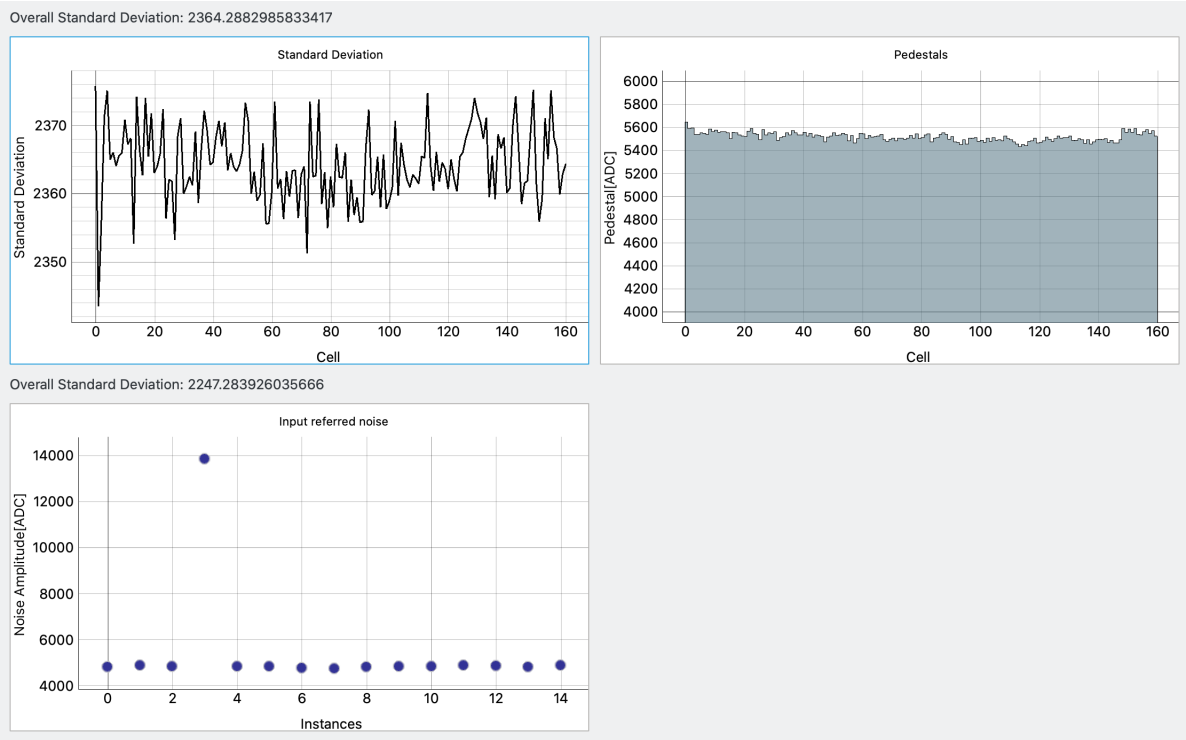

Figure 27 – An example of a calibrated cathode channel. Top left graph displays the standard deviation for each cell. Bottom left graph displays all instances of recorded input referred noise and top right graph displays pedestals for each cell.

5.4 Step 2: Process Data

The *process data* layout is presented in figure 28. This part of the software processes source-data produced by the *Testbench* and creates and displays a finished spectrum.

Figure 28 – Interface layout of the process data function

The processing sequence is presented in figure 29. To start logging events the *Start*

Logging pushbutton must be pressed. After initiating, a new thread will open the latest recorded file in a specified path and wait for data. If no data is received, it will wait for 3 seconds and try again. If data is received, the data is translated into Pandas's DataFrame and further processed by subtracting pedestals. The signal amplitude is found by applying a pulse-height filter, as explained in 2.5, and further multiplied with a gain factor. All events with corresponding timestamps are added together, and binned to update the existing histogram.

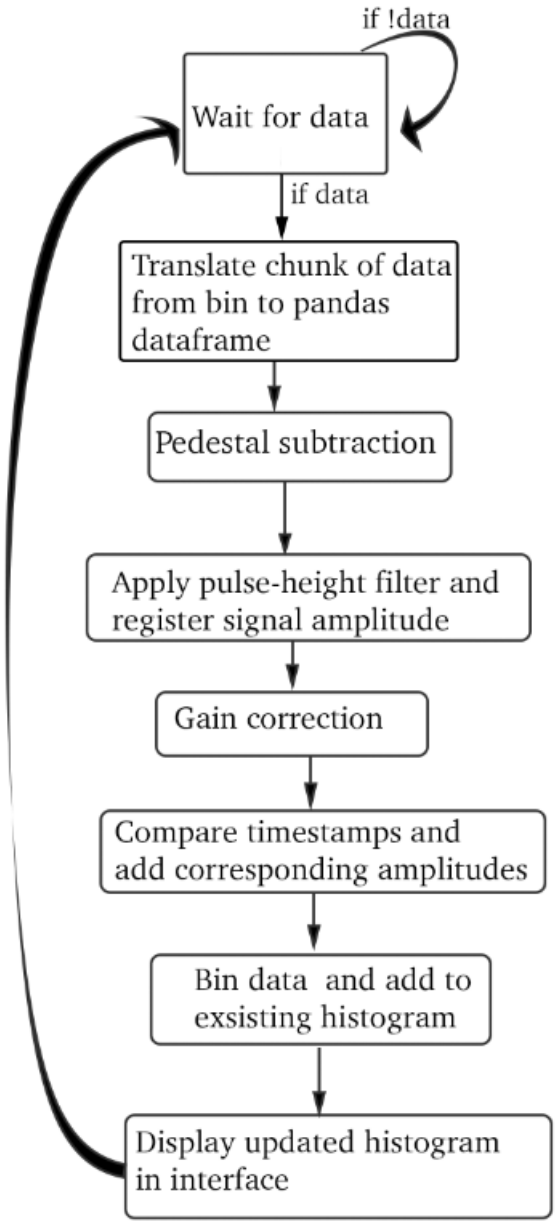

Figure 29 – The processing sequence of data within the calibration software.

Since the interface reads data as it is written, a close to "real-time" readout is created, which allows the user to get instant feedback when tweaking system settings or setup. There are however some limitations with this process, since the data can only be read as fast as the software are able to process the data. Hence, for large amounts of new data there is a delay in processing. A workaround has been implemented with the option to skip to the end of the file, so that any new data that processes

will be "fresh" data. The user also have the option to clear the current spectrum so that any changes in spectral resolution from new system settings or setup are easy to differentiate.

The main feature of this layout is the graph which displays the finished energy spectrum, which is constantly updated as the algorithm processes more data. The option called *Single Event Spectrum* will create a new window as depicted in figure 30 with a histogram containing exclusively single interaction events. A similar window can be called with the *Edge Pixels Spectrum* and *Corner Pixels Spectrum* buttons which contain edge pixels and corner pixels respectively.

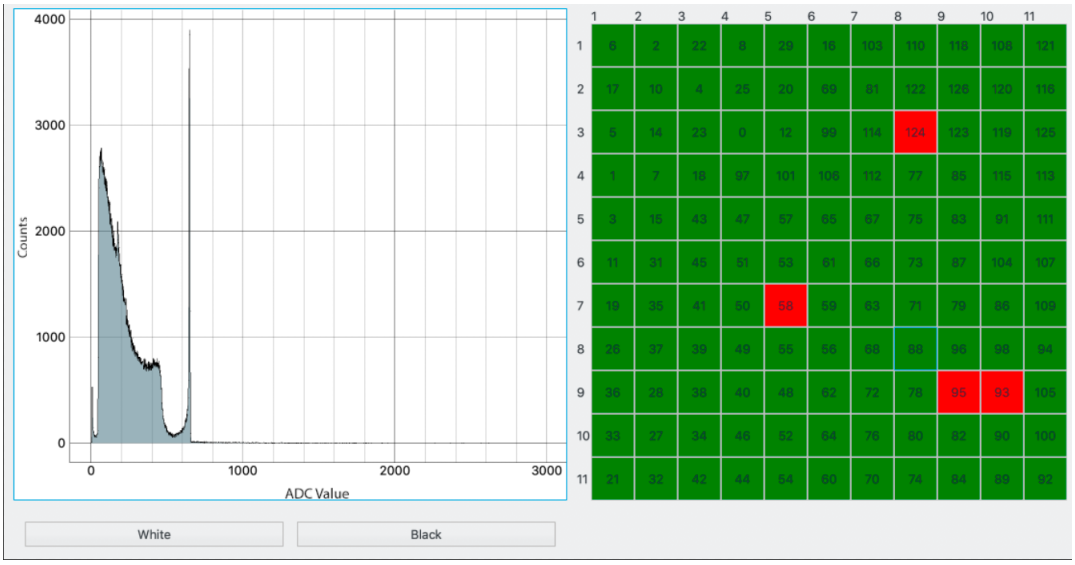

Figure 30 – Window for single event spectrum, which contains a histogram of the single interactions event(left) and a selection pixelmap. When a pixel is pressed the corresponding events will be subtracted(red pixel) or added(green pixel) to the spectrum. The numbers displayed on each pixel correspond with the channel number.

To inspect the quality of logged events there is the option to visualize data in detail. The interface will pull an event from the current DataFrame processing and display it as depicted in figure 31. All interactions with identical timestamps are graphed, including the cathode event. The events are graphed after pedestal subtraction, and corresponding coordinates are highlighted in yellow within the pixelmap. The highlighted pixels will display also the corresponding recorded amplitudes. This allows for effective investigation of the data in detail, such as readout errors, quality of the data, any abnormalities. It would also show if there is any error in the processing step such as misaligned pedestals.

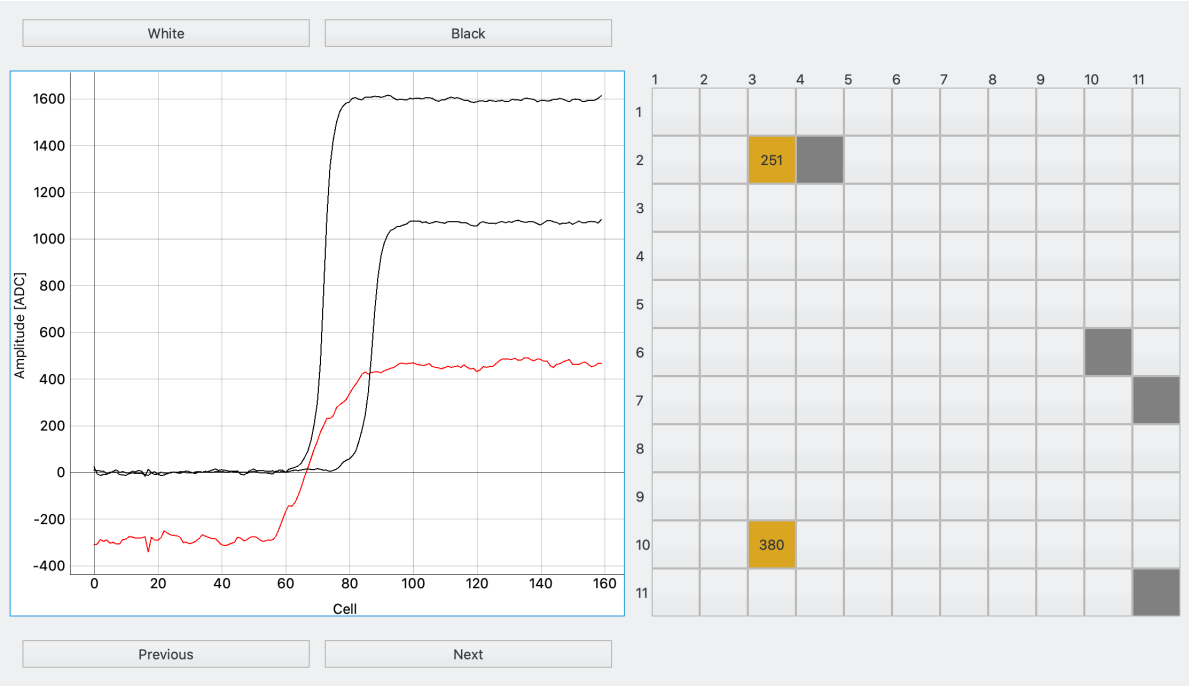

Figure 31 – Window displaying an event from the current DataFrame. The graph to the right displays each event including the cathode data in red (if present). The pixelmap displays the coordinates and amplitude of the signals in yellow.

The pixelmap in the main window displays the current amount of registered events of each channel. Any ”dead” channels, i.e no registered events, will quickly be noticeable. Each pixel can be pressed to open a new window as depicted in figure 32. The window includes a histogram of events exclusive to that channel. There is also the option to enter peak value which will be used for peak alignment as explained in section 4.2.2. If enough entries, the channelspectrum FWHM can be calculated and displayed by pressing the *FWHM* pushbutton. If a peak is located in the FWHM calculation it will automatically be displayed in the peak value window.

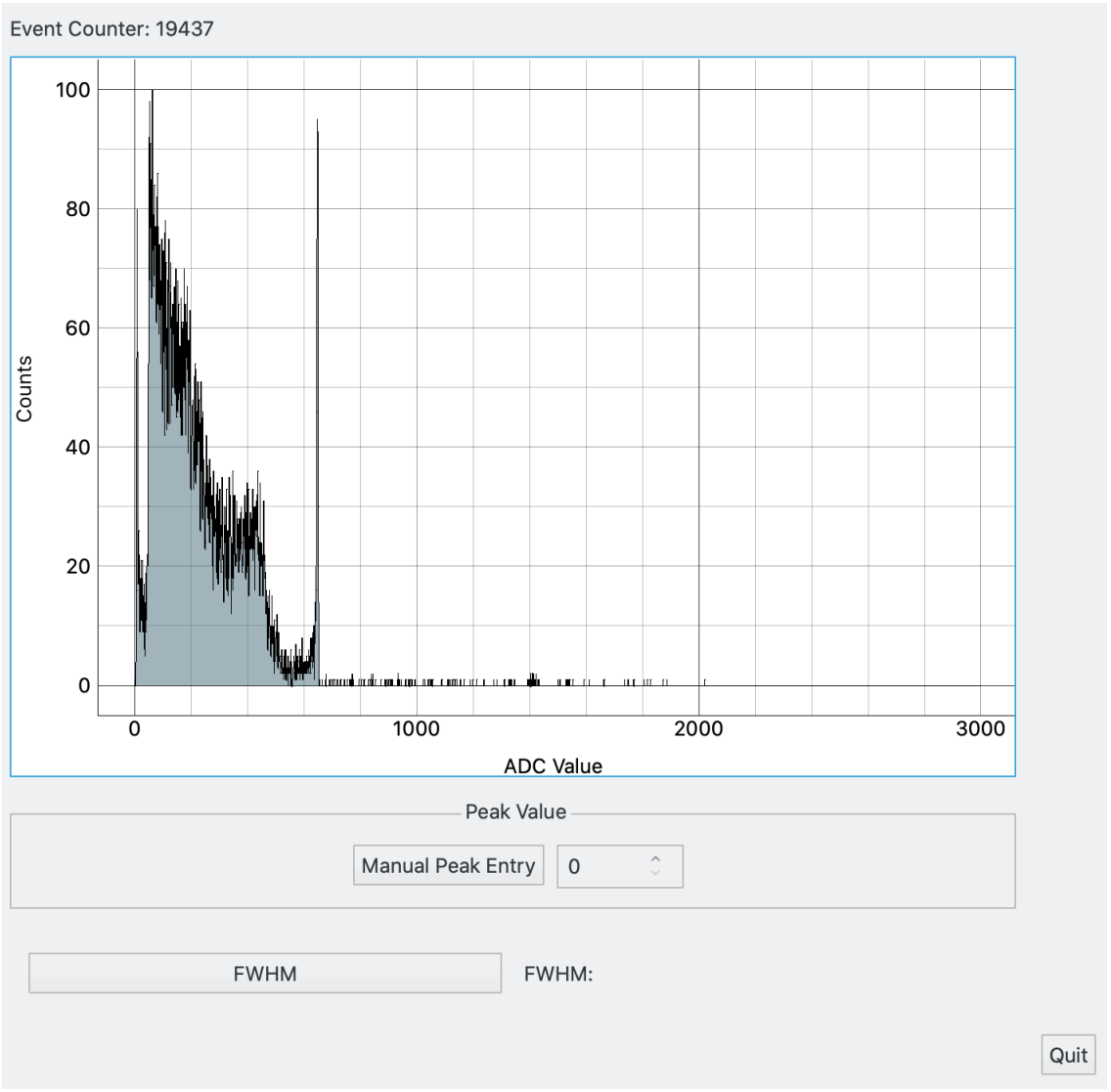

Figure 32 – Pixel window that include a histogram of data within that pixel, either all events or only single interaction events. The peak value can manually be entered in Manual Peak Entry. If enough data the FWHM will be calculated and displayed, by pressing the *FWHM* pushbutton. If a peak is located in the FWHM calculation it will automatically be displayed in the peak value window.

Two options follow: to either display only single interaction events or all events in the channel spectra. The choice will change the histogram within the pixel window and the displayed registered events in each pixel. It is simply changed by clicking the desired display option as depicted in figure 33.

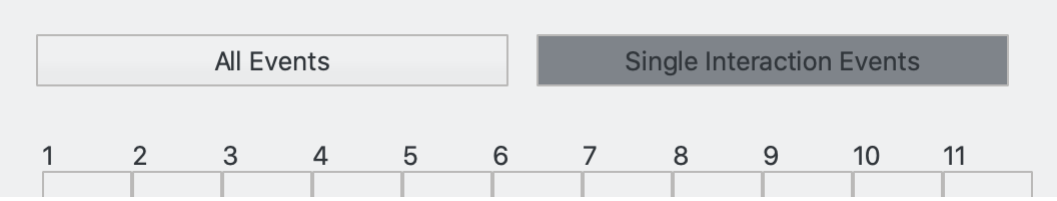

Figure 33 – Pushbuttons to either choose to display all events or only single interaction events in the channel spectra.

All graphs are made using the library *PyQtGraph* which is a Scientific Graphics and GUI Library for Python [24]. The graphs have built in features such as displaying the graph logarithmic and to export the graph to *matplotlib* or a csv format. The features can be accessed by right clicking the axis, as depicted in figure 34

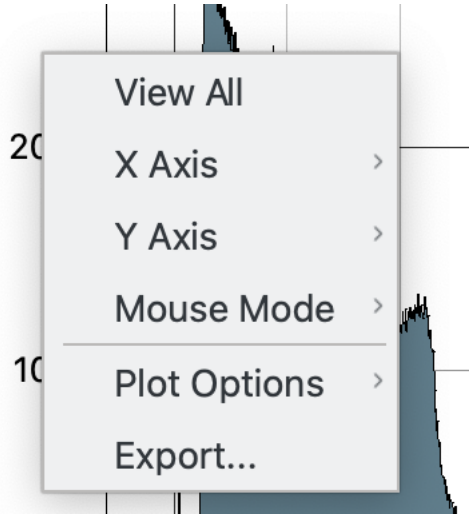

Figure 34 – Built in features in the *PyQtGraph* library.

5.5 Discussion

The GDS-100 Calibration User Interface has been successfully implemented. It is not directly implemented in the already existing *Testbench* due to limited support of *Python* libraries. This makes it possible to run the interface separate from the *Testbench* on already logged data. The *Testbench* only support Windows while the interface can easily be adapted to other operating systems. The interface is implemented using the python library PyQt5. This library is accessible and heavily documented, which makes it easy to customize by the user if additional features are required or any existing features can be adapted to the user's needs.

The interface is currently implemented for one ASIC-module. This can easily be replicated for all four, however further development should include a common spectrum which collects data from all ASIC-modules. The expansion to all ASICs will require more data processing. Further development should also explore methods to accelerate the data processing time.

The calibration routine calculates noise and pedestals and gives the option to calculate gain factors using the internal calibration pulse within the system. The second option to use peak alignment is not fully automated as the user must manually add peak values. A fully automated calibration routine with peak alignment should be further explored.

The interface makes it possible to see explicit data from single event interaction, from each channel and for corner and edge pixels. Further development should include categorization of Compton-scattering events and charge sharing events.

6 Testing

This chapter are divided into four sections. The first section will introduce the laboratory setup. The second section determine the linearity of the system using an internal calibration pulse and an external pulse generator. Section three examine the performance of the calibration routine and compare resulting energy spectrum. The last section discusses the results.

6.1 Laboratory setup

A diagram of the laboratory setup for collecting source code is depicted in 35

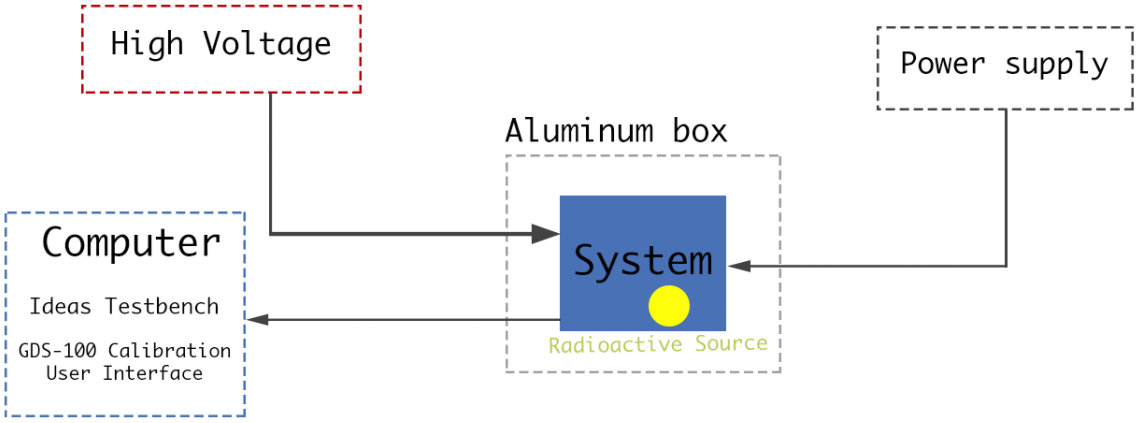

Figure 35 – A diagram of the laboratory set-up.

The system is placed inside an aluminum box to prevent light from triggering the system, the box is also grounded to minimize noise. The sources are placed above the detector. Sources with low activity should be close to the detector, but with some spacing to allow more uniform interaction within the crystal. A more active source should be placed further away as not to saturate the pixels. The system is connected to a computer with the Testbench and software running simultaneously. A power source and high voltage is also connected to the system. The high Voltage is 2500V for all measurements in this thesis. The laboratory setup is depicted in figure 36.

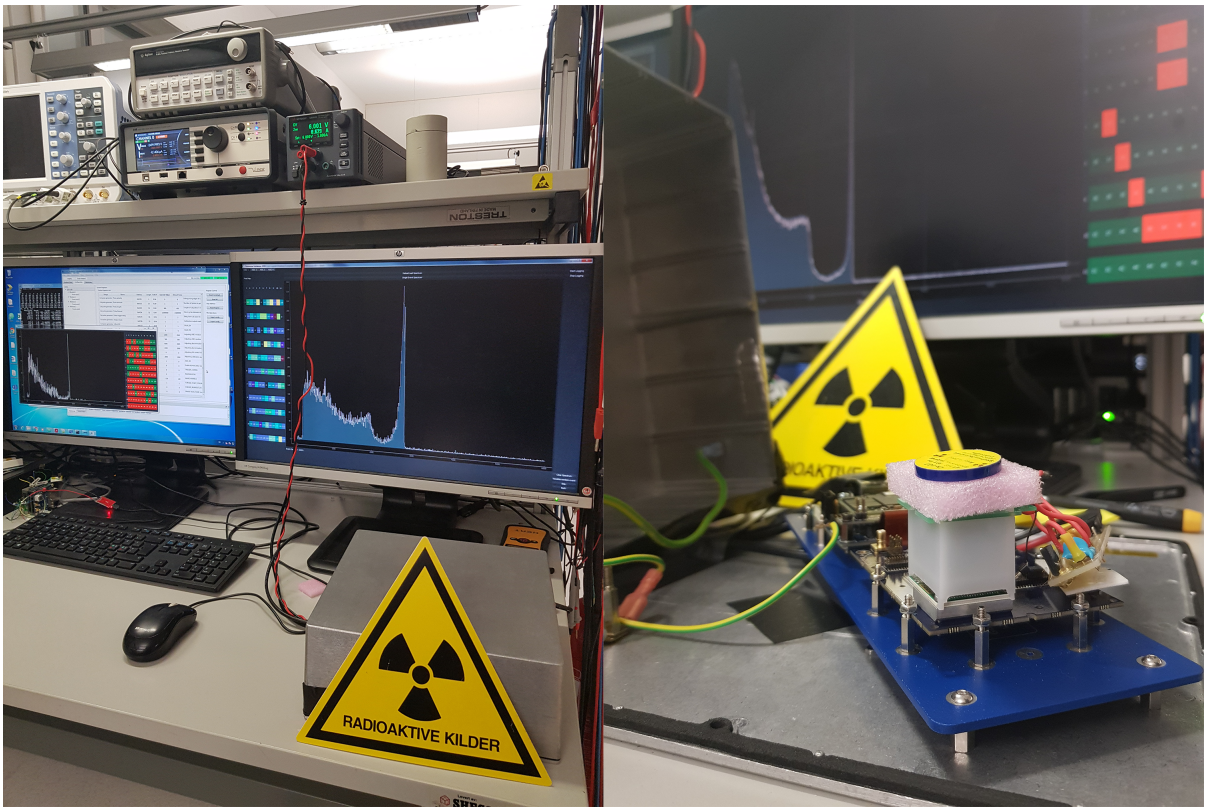

Figure 36 – Overall lab setup with the GDS-100 system placed under an aluminum box connected to a power-supply, high voltage generator and computer (right) and system inside the box with Cs^{137} source. (left)

The specific components used in this project are listed in table 2.

Table 2 – Laboratory Components

Type	Name
High Voltage Supply	iseg SHR 22 60 Switchable High End High Precision AC/DC Desktop HV Source-Measure-Unit
Power Supply	Keysight E36102B Laboratory DC Power Supply 1 Ch
Oscilloscope	ROHDE & SCHWARZ RTB2004 Digital Oscilloscope 4 channel 200MHz
Function generator	Agilent 33120A Arbitrary Waveform Generator
CZT crystal	Redlen 15mm CZT

The sources used are disk sources of Cs^{137} and Na^{22} with an activity of 0.1μCi and 1μCi respectively. The sources used are depicted in figure 37

Figure 37 – Disk sources of Cs^{137} and Na^{22}.

6.2 System linearity

As described in 4.2.2, the linearity of the system can be tested using the internal calibration pulse. The pulse simulates the current from a radioactive source, but with programmable amplitude. There will, however, be uncertainties as the calibration pulse will introduce additional electronic noise. This chapter describes two tests done to determine this uncertainty and the linearity of the system. The two tests are as following:

1. Use internal calibrating pulse with incremental pulse heights and measure with oscilloscope at the output.

2. Use external pulse with incremental pulse heights and measure with oscilloscope at the output.

The circuit diagram of the internal calibrating test pulse is depicted in figure 38. The depicted circuit is the relevant part of a more comprehensive circuit that can be found in appendix B. There is the option of small pulse range or large pulse range by adjusting the attenuation which is done by connecting JH2.

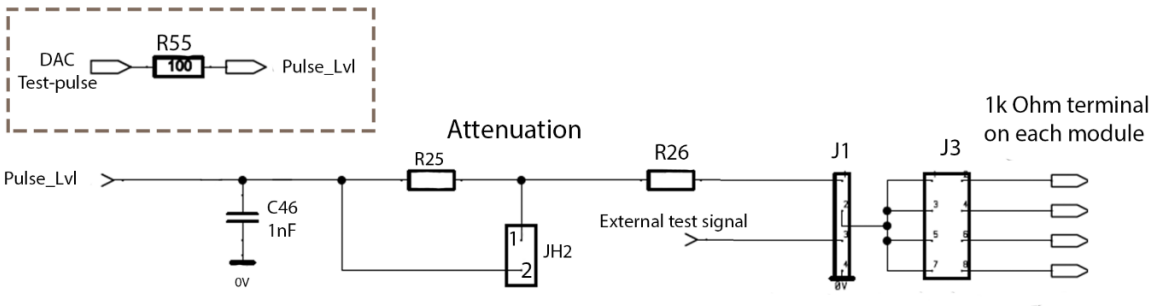

Figure 38 – Simplified circuit diagram of the internal calibration pulse generator.

Initial testing measured range of 0-533mV and 0-1823mV for small and large pulse range respectively. The intended ranges are 0-100mV and 0-1000mV. The termination on the ASIC-modules are 1000Ω, however, the initial components in the design depicted in figure 38 were based on an old design with a termination of 100Ω. Using voltage division (15) the new ideal component values for $R25$ and $R26$ are calculated to be $R25 = 22\text{k}\Omega$ and $R26 = 1.4k\Omega$ when taken into account $R55$ and the termination resistance.

$$V_{out} = V_{in} * \frac{R_2}{R_2 + R_1} \tag{15}$$

Figure 39 depicts the measured outputs fitted with a linear fit using linear regression. The maximum residual from the linear fitting divided by the dynamic range quantifies the non-linearity[18]. The non-linearity is thus calculated to be $\approx 0.85\%$ and $\approx 0.74\%$ for the ranges (0-100mV) and (0-1000mV) respectively.

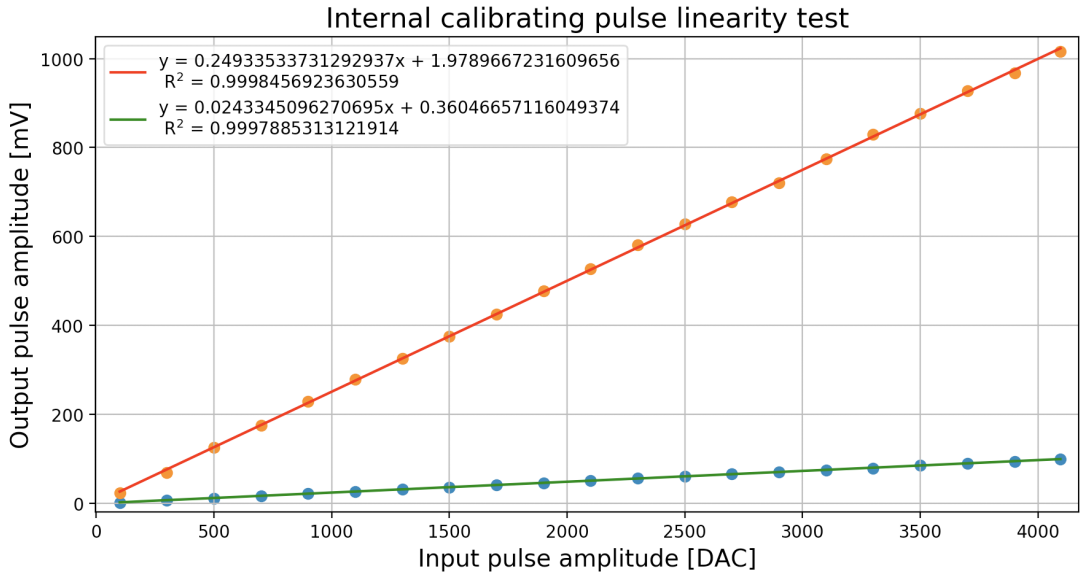

Figure 39 – Linearity plot of internal calibrating pulse for ranges 0-100mV(blue dots) and 0-1000mV(orange dots). The corresponding linear fittings are represented by the red and green lines.

Test 2 was carried out with an external test pulse. Figure 40 represents the linearity with increasing signal amplitude. The external pulse gives a non-linearity of $\approx 0.2\%$ for the measured range.

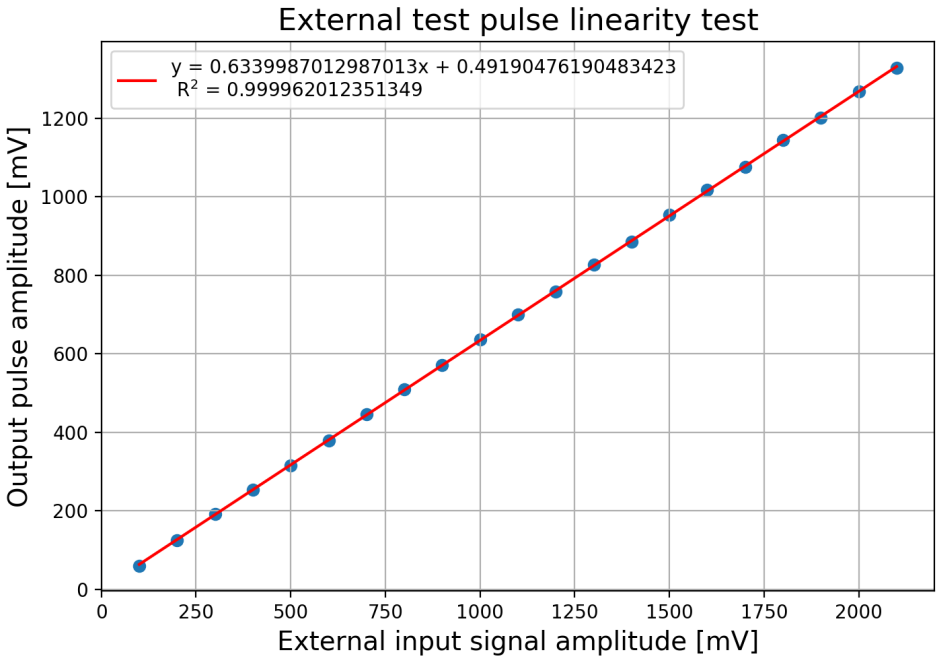

Figure 40 – Linearity plot with external pulse signal(blue dots) with corresponding liner fitting(red line).

The linearity of the internal calibrating pulse is lower than the external pulse as expected, as the external pulse signal introduces less noise into the system. The system does however show excellent linearity.

6.3 Performance of Calibration Routine

Noise and Pedestals Two measurements of pedestal readouts were taken, one with high voltage connected and one without. The resulting calculations for noise and pedestals, using 1000 baseline readouts per channel, are depicted in figure 41 and figure 42 respectively. The input referred noise amplitudes were calculated using the trapezoidal filter with $\Delta t_G = 14$ samples and $\Delta t_L = 70$ samples. Key values of both cases are presented in table 3.

Figure 41 – Input referred noise and pedestal calculation from 1000 baseline readouts per channel. High voltage connected.

Figure 42 – Input referred noise and pedestal calculation from 1000 baseline readouts per channel. High voltage not connected.

Table 3 – Key Values From Pedestal and Noise calculation

Anodes		
Values	**With HV connected**	**Without HV connected**
Input Referred Noise (All Channels) [ADC]	8.433	3.123
Standard Deviation (All Channels)[ADC]	10.313	6.712
Cathode		
Values	**With HV connected**	**Without HV connected**
Input Referred Noise [ADC]	1880.973	19.343
Standard Deviation [ADC]	1912.50	25.647

Pedestal subtraction using the pedestals calculated with and without HV are compared in figure 43.

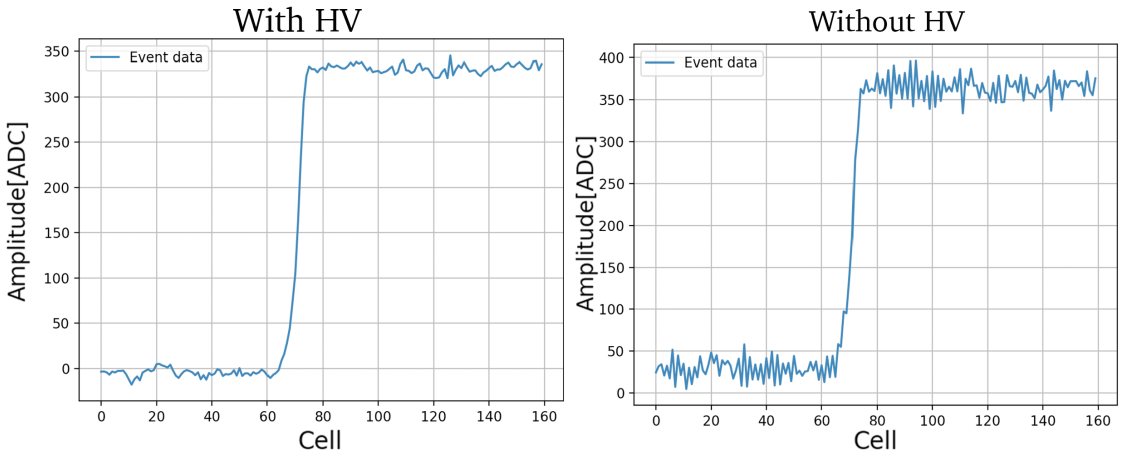

Figure 43 – A comparison of pedestal subtraction performed with pedestals calculated when HV is connected(left) and HV is not connected(right)

Figure 41 shows an exceedingly large amount of noise in channel no.61 with coordinates (6,6). The cathode channel is connected to the crystal with conducting glue directly above channel no.61 which could indirectly induce noise in that pixel. A comparison of channel no.61 and one of its neighboring channel no.53 (6,5) with approximately the same amount of data is depicted in figure 44. The spectra indicates a poor spectral energy resolution in channel no.61.

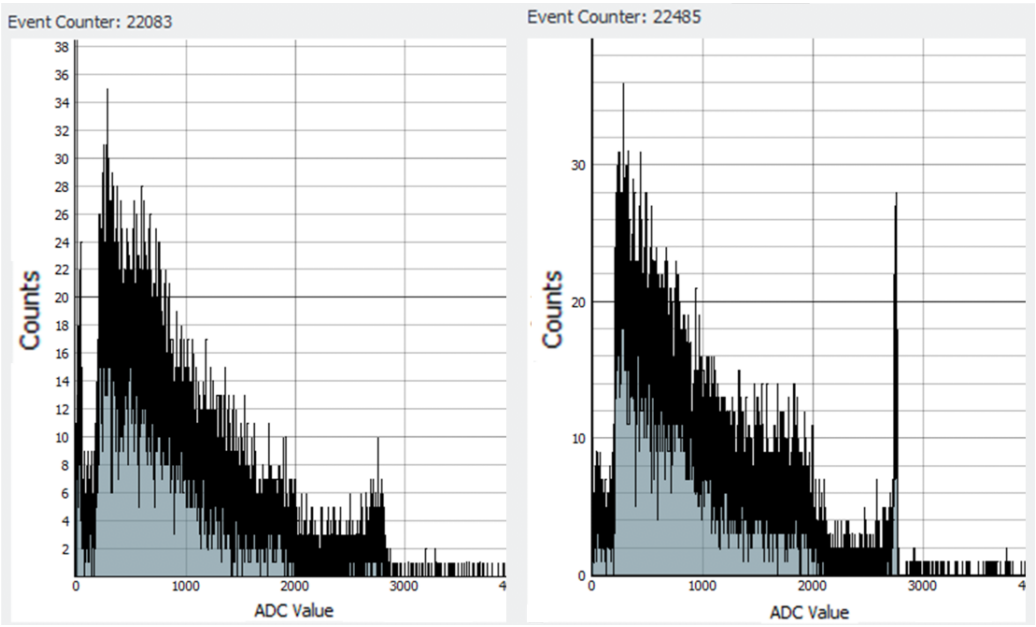

Figure 44 – Spectrum from channel no.53 with coordinates (6,5)(left) and no.61 with coordinates (6,6)(right), to compare a channel with average noise contribution and exceedingly large noise contribution. Bin-width = 1

The spectrum of Cs^{137} after pedestal correction resulted in a FWHM of 3.257% and is depicted in figure 45. The spectrum containing only single interaction events resulted in a FWHM of 1.045% and is depicted in figure 46.

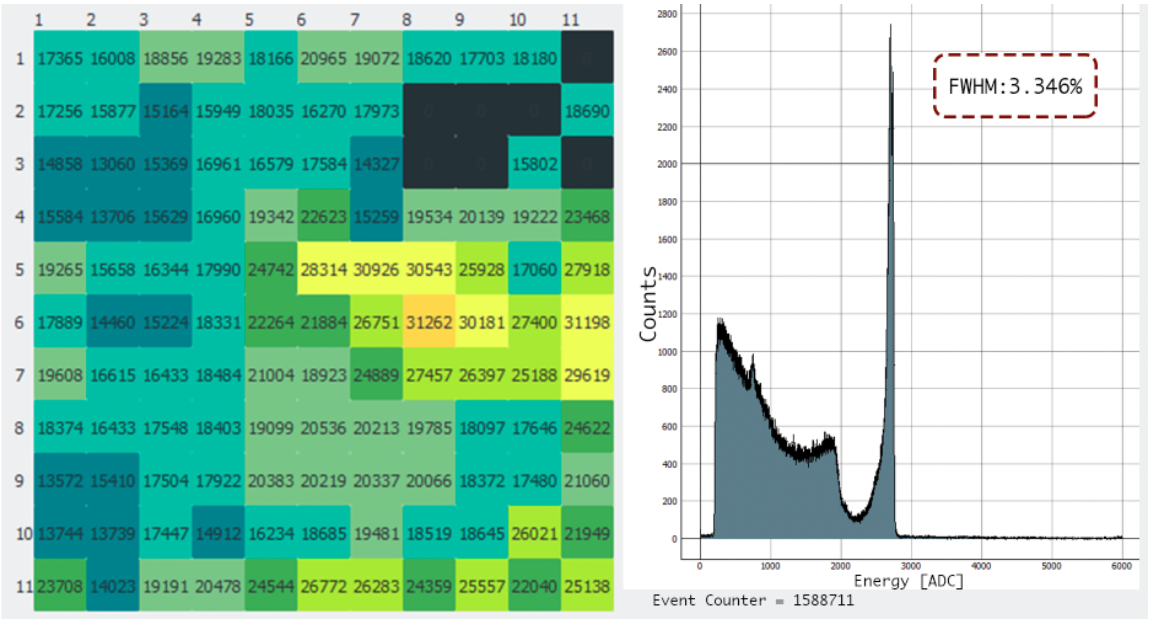

Figure 45 – Cs137 spectrum after pedestal correction. FWHM: 3.346%. Number of interaction equal to 0 means bad pixel or poor photopeak. bin-width:1. System settings are presented in appendix D

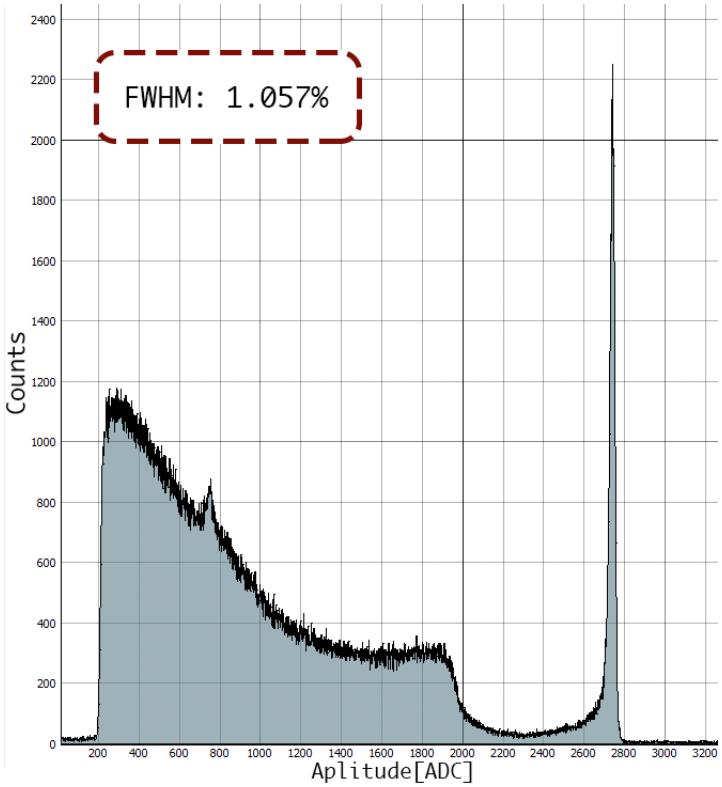

Figure 46 – Cs^{137} spectrum after pedestal correction with only single interaction events. FWHM: 1.057%. Bin-width: 1. System settings are presented in appendix D

Gain Correction As described in 4.2.2 there are two suggested methods for gain correction: 1) Internal calibrating pulse 2) Aligning channel spectra peaks.

Using the first method, gain factor calculations using the internal calibrating pulse are depicted in figure 47 with corresponding distribution of gain factors. 1000 readouts for each channel was used for the calculation with an average standard deviation of 4.35 ADC values.

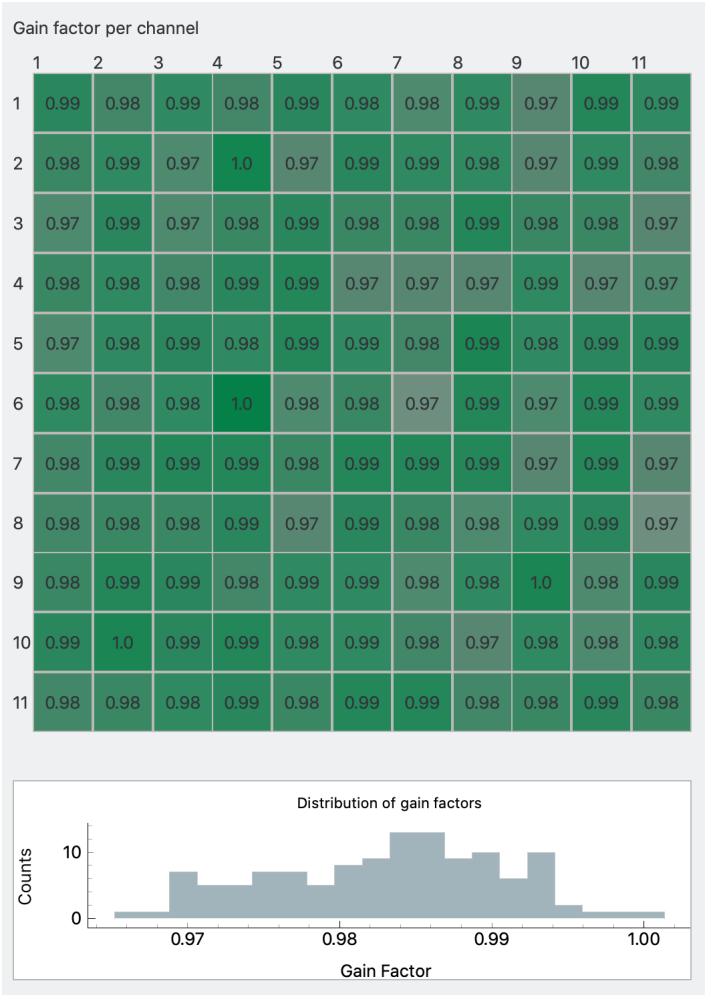

Figure 47 – The pixelmap represent the resulting gain factors from using the internal calibration pulse readout. Each pixel represent the gain factor for the channel with corresponding coordinates. The histogram depicts the distribution of gain factors.

The spectrum of Cs^{137} after pedestal and gain correction using the internal calibrating pulse resulted in a FWHM of 3.262% and is depicted in figure 48. The single interaction spectrum resulted in a FWHM of 2.565% and is depicted in figure 49.

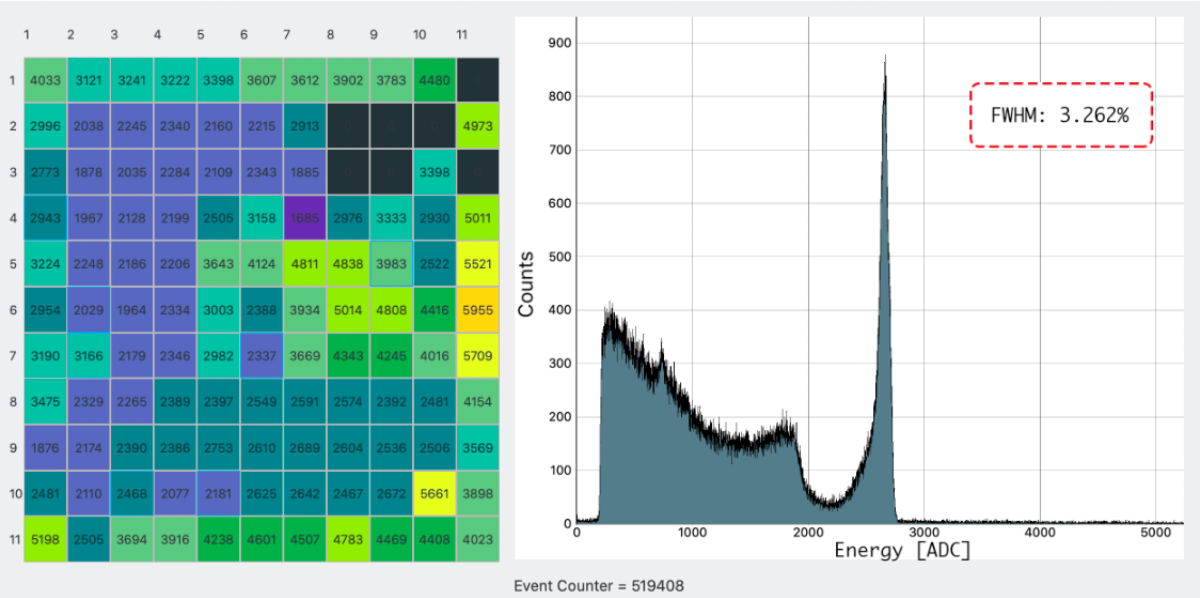

Figure 48 – Cs^{137} spectrum after pedestal and gain correction using the internal calibration pulse, and corresponding pixelmap displaying the amount of interactions in each channel. Number of interaction equal to 0 means bad pixel or poor photopeak. FWHM of 3.626%. Bin width: 1

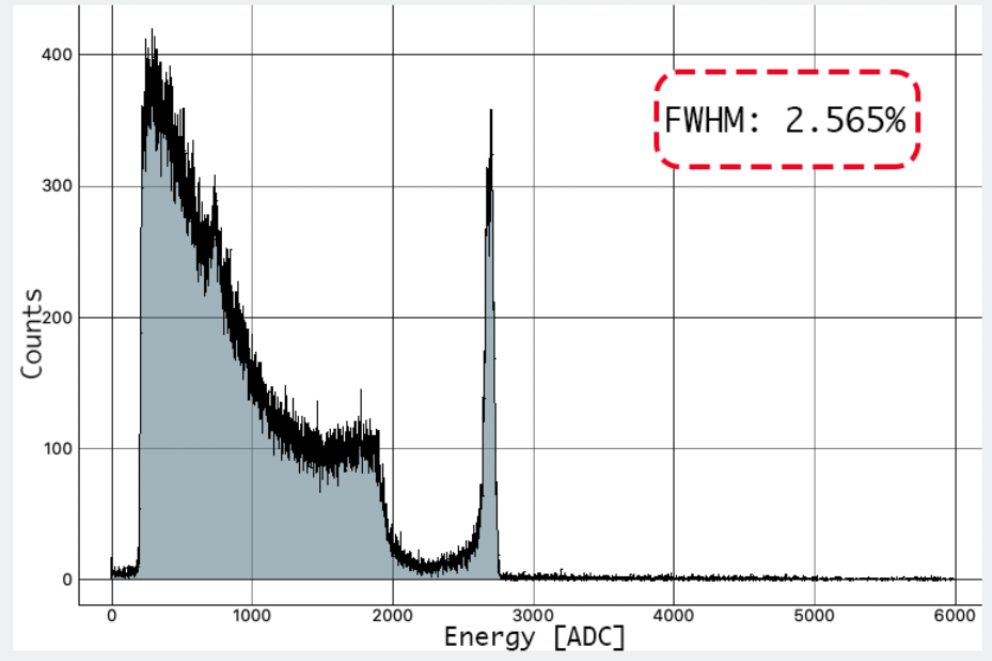

Figure 49 – Single interaction Cs^{137} spectrum after pedestal and gain correction using the internal calibration pulse. FWHM: 2.565%. Bin width: 1

The second method was performed using two sources: Cs^{137} with theoretical peaks at 662keV and Na^{22} with its two peaks at 511keV and 1274keV. Spectra of both sources were calculated for each channel, and entered manually from inspection via the interface. Initially, there was an intention of using both peaks of Na^{22} but the sharp second peak shown in figure 50 suggests saturation for high energy peaks, which

is a result of too much gain in the preamplifier. Hence, only the main 511keV and 662keV peaks were used.

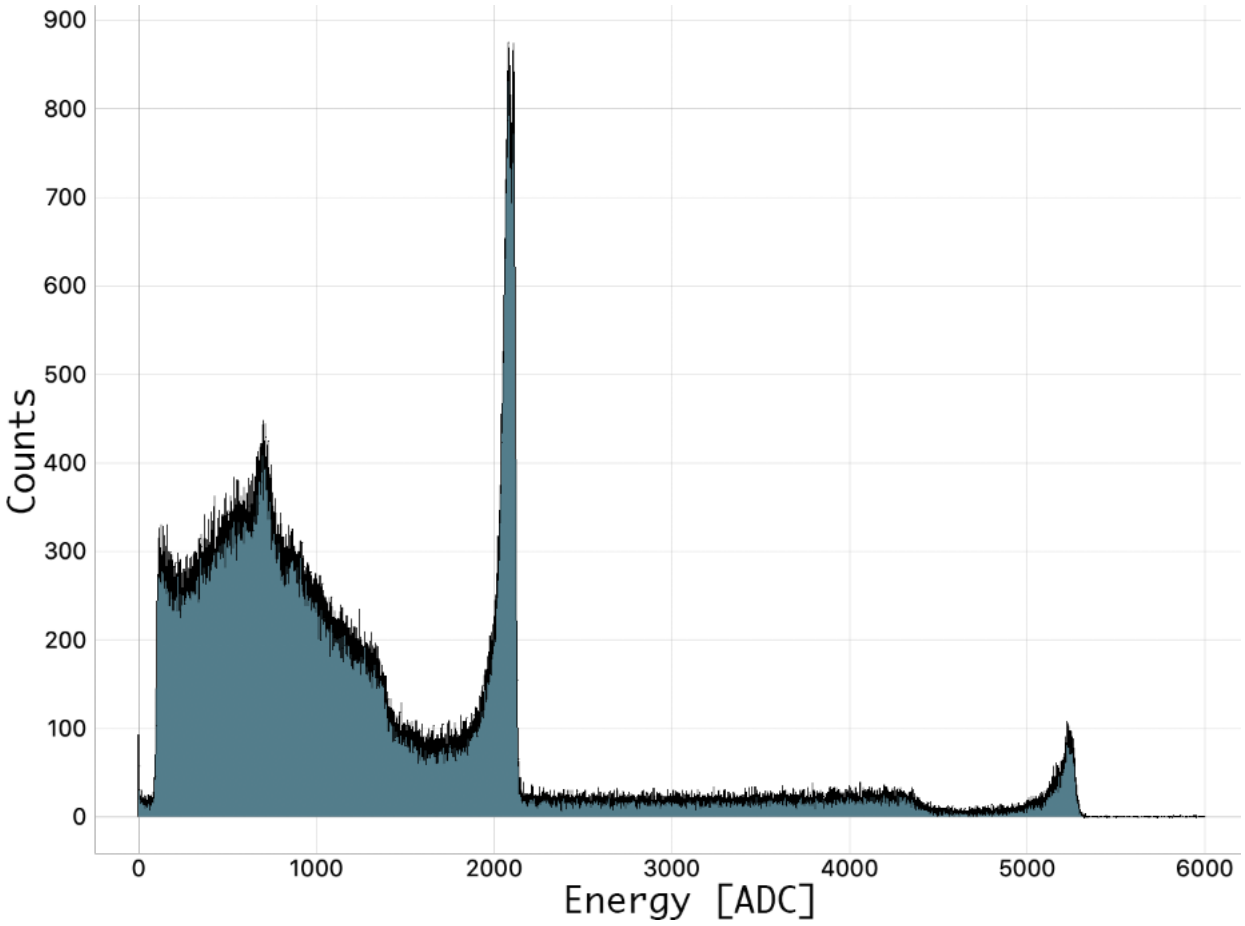

Figure 50 – Na^{22} spectrum with multiple interaction readouts. System setting can be found in appedix D

Figure 51 depicts a visualization of gain differences and the gain factor distribution.

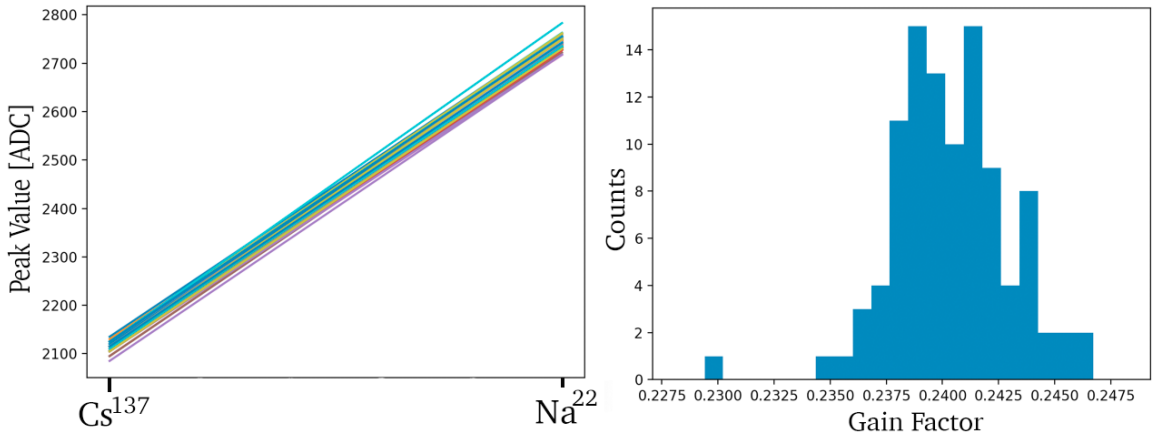

Figure 51 – A visualization of gain differences where each line represents its gain of one channel (left) and a distribution of the resulting gain factors.(Right)

The resulting spectrum of Cs^{137} after pedestal and gain correction, employing the

second method, is depicted in figure 52. The spectrum has a FWHM of 2.72%. The single interaction event spectrum with FWHM 0.755% is depicted in figure 53.

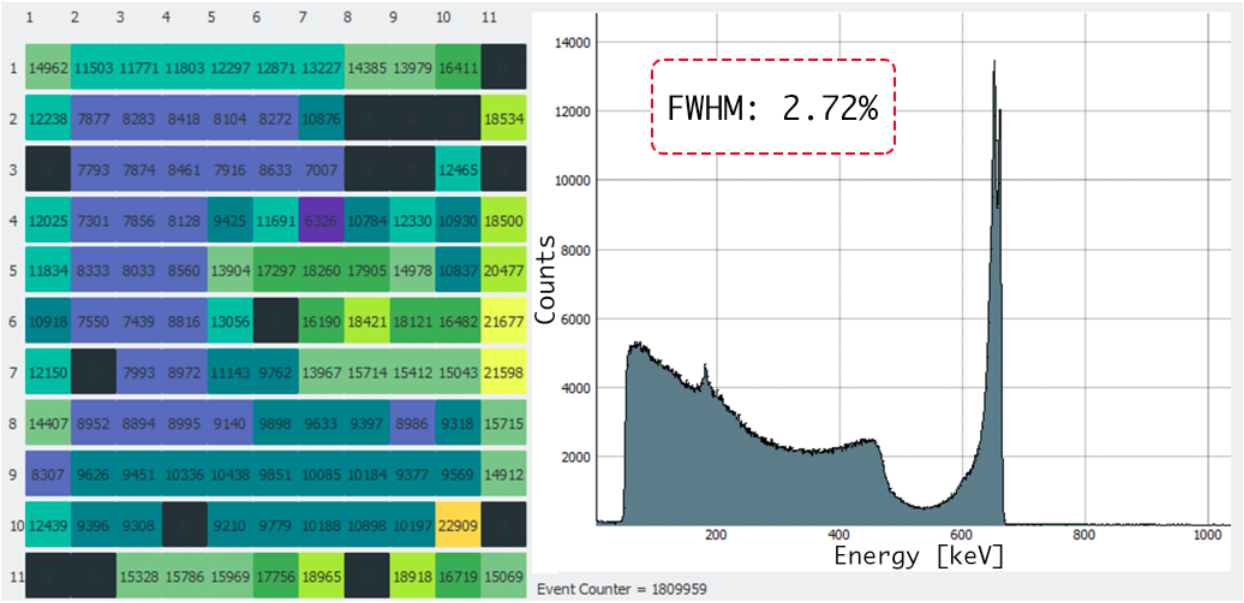

Figure 52 – Cs^{137} spectrum after pedestal and gain correction using peak alignment and corresponding pixelmap displaying the amount of interactions in each channel. FWHM: 2.720%. Bin width: 1. Number of interaction equal to 0 means bad pixel or poor photopeak.

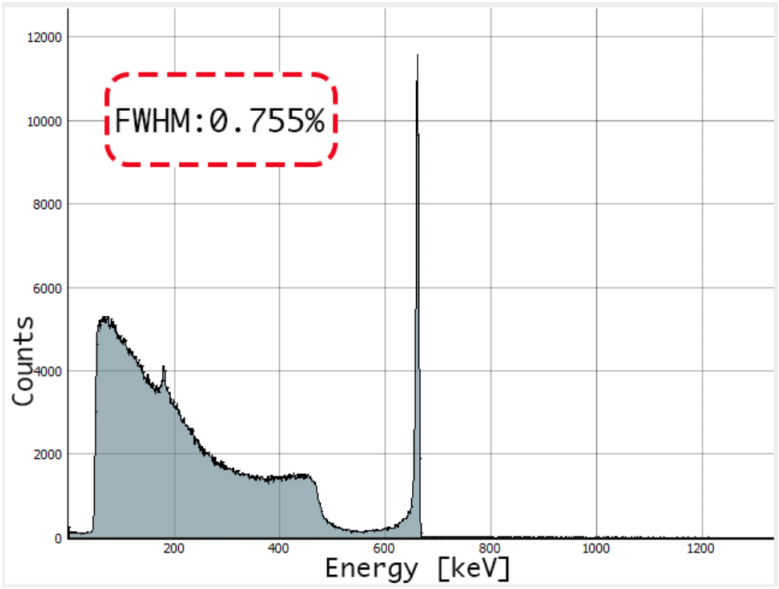

Figure 53 – Single interaction Cs^{137} spectrum after pedestal and gain correction using peak alignment. FWHM: 0.755%. Bin width: 1

6.3.1 Pulse Height Analysis

The two methods suggested for pulse height analysis are the traditional trapezoidal filter and using Gaussian Mixture Models. An in depth analysis was done in the specialization project [1]. The 3D-GMM method and the trapezoidal filter with $\Delta t_L =$

70 samples and $\Delta t_G = 14$ samples performed best, and were also tested with the new system. The results are presented in table 4.

Table 4 – Results from pulse height analysis

Pulse-height Analysis Method	FWHM
Trapezoidal Filter	0.923%
3D-GMM	0.755%

6.4 Discussion

Noise and Pedestals Readouts with HV connected show overall significantly higher noise, as to be expected as the HV introduces noise into the system. The readout with HV connected gives a more accurate pedestal subtraction as it is closer to the state of which radioactive source data is logged. By evaluating the noise readouts, a channel with poor spectral energy resolution was successfully identified. Channel no.61, which shows high levels of noise, is directly located below the cathode channel that can indirectly induce noise on that pixel. Further investigation of the hardware solution should be done.

Gain Correction The first method of gain correction is effective as it does not need any source-data, only a readout of calibration pulses. It resulted in a small improvement in the multiple interaction spectrum, but lower spectral resolution in the single interaction spectrum. This suggests a high uncertainty in the internal calibration readouts. The 1000 readouts used in this calculation had an average standard deviation of 4.35 ADC values across channels. A larger amount of readouts could result in higher accuracy. There are however other sources of errors that need to be addressed. The measurements were taken without the high voltage as it added too much noise. Just as with the pedestal measurements, this does not give an accurate representation of the state of the system when logging source data. Further development should introduce better classification of the data so to filter out bad readouts. Another source of error is introduced by the pulse-height filter which estimates the signal amplitude. The physical placement of the internal calibration pulse generate might also introduce a slight voltage drop for the channels further away.

The second method was shown to be more accurate, however it is not as fast to calculate. For each radioactive source used, a spectrum must be recorded for each channel, and have enough data to correctly identify the energy peak. The gain factors where calculated from single interaction events within each pixel in order to minimize any added source of error from gain-variations in neighboring channels. This does however mean that any energy leaked into neighboring channels below the trigger threshold is lost, resulting in a slightly skewed peak. Other physical effects such as depth interaction might also skew the results. This method is also based on the assumption of linear gain, as the system shows excellent linearity measured in 6.2. However, there could be slight variations between channels and between gain settings which should be further explored. Further work should also include more reference points, i.e more radioactive sources, for higher accuracy. This method is only partly automated in the calibration interface as it is possible to visualize each channel spectrum, but the user has to manually record each peak value. Further

development should include a more automated system for calculating the peak values and apply the gain factors to the new data.

The single interaction spectrum with FWHM 0.775% shows great improvement from the raw data. This result is exceptional, as only pedestal subtraction and gain correction have been done. The result does not compare to previous work of 0.48%, but show great potential for future work.

The multiple interaction event spectrum shows only a small improvement from raw data. The main contributor of the poor spectral resolution is high threshold, which results in losing neighbor-data. There is a prominent division in the 662keV peak as depicted in 54 where the magnitude appears to correspond to the energy lost below the threshold, estimated to be 40keV in this measurement.

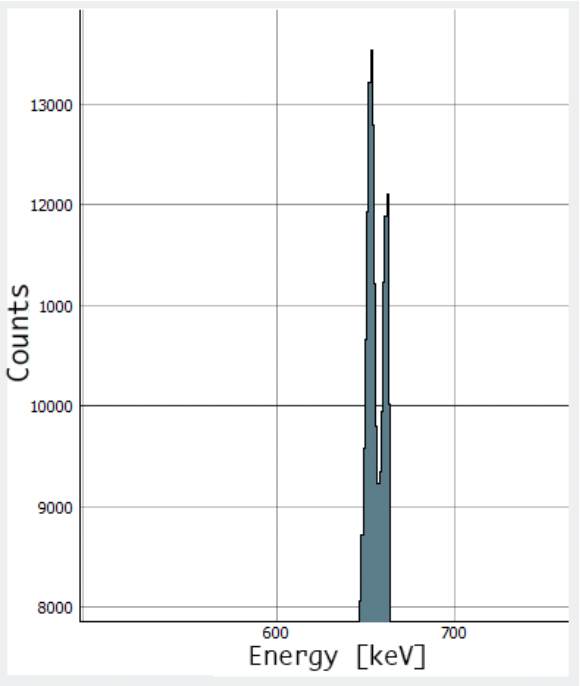

Figure 54 – Close-up of the multiple events Cs^{137} 662keV peak.

Future development should include all neighboring channels in each readout. In order to benefit from this adjustment, accurate noise classification is crucial, as well as optimizing the pulse-height filter for neighboring channels to accurately estimate signal amplitude. Neighboring signals are highly dependent on where in the pixel the energy is absorbed, and be used to uncover sub-pixel position[18] to further improve energy resolution. Further development should also include to optimize hardware and system settings.

The 3D-GMM outperfomed the traditional trapezoidal filter as the 3D-GMM resultet in a FWHM: 0.755% and the trapezoidal filter in FWHM: 0.923%. However, the choice of shaping time Δt_L and peaking time Δt_G was based on the result of the work done in the specialization project. Further work should explore to optimize the trapezoidal filter specific to the GDS-100 system.

7 Depth Correction

To improve spectral resolution, depth correction of single event interaction using C/A-ratio was performed. Depth correction was not implemented in the calibration software, but used as an additional effort to improve spectral resolution due to the timeframe of the project. This section will present the depth correction implementation and discuss the results.

As explained in section 2.4, the cathode to anode amplitude ratio can be used to find depth of interaction of a gamma radiation event within a CZT-crystal. A spectrum of raw data was divided into subspectra dependent on C/A-ratio as depicted in figure 55, and a factor for each depth increment was calculated. A heatmap of the subspectra is depicted in figure 56.

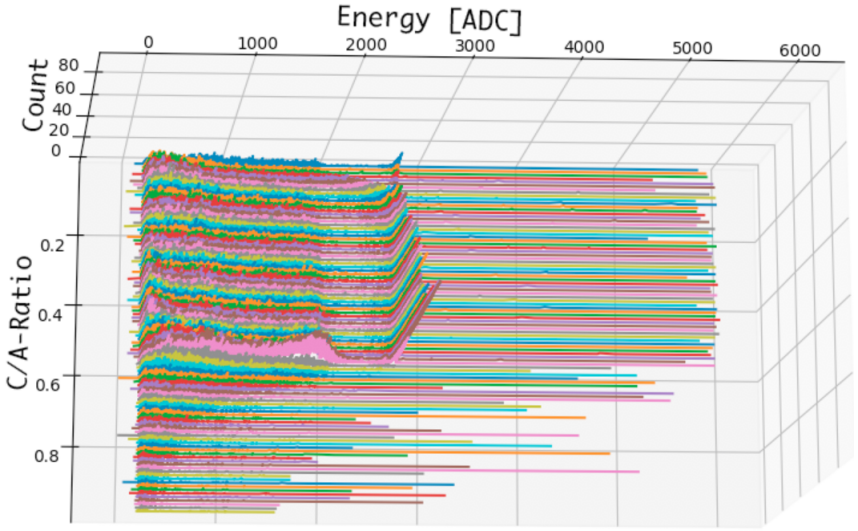

Figure 55 – A spectrum divided into subspectra based on C/A-ratio.

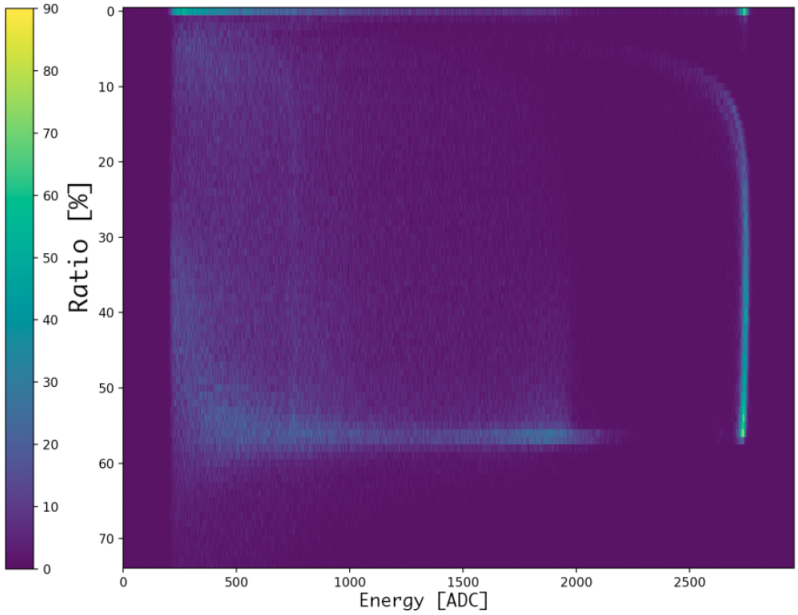

Figure 56 – Heatmap of a spectrum divided into subspectra based on C/A- ratio.

As expected, the peak-energy is lower closer to the 0 ratio, i.e closer to the anode pixels. However on the zero mark, there is an anomaly of high energy peaks, which could be caused by noisy cathode events or faulty readouts interpreted as low energy or zero amplitude events, and hence not correctly categorized by the algorithm. In further calculations these peaks are excluded.

As recorded in table 3 the cathode channel has significantly higher noise contribution than the anode signals which is translated into noisy cathode events. An example of such an event is depicted in figure 57. Noisy cathode events will introduce uncertainty when used for depth correction.

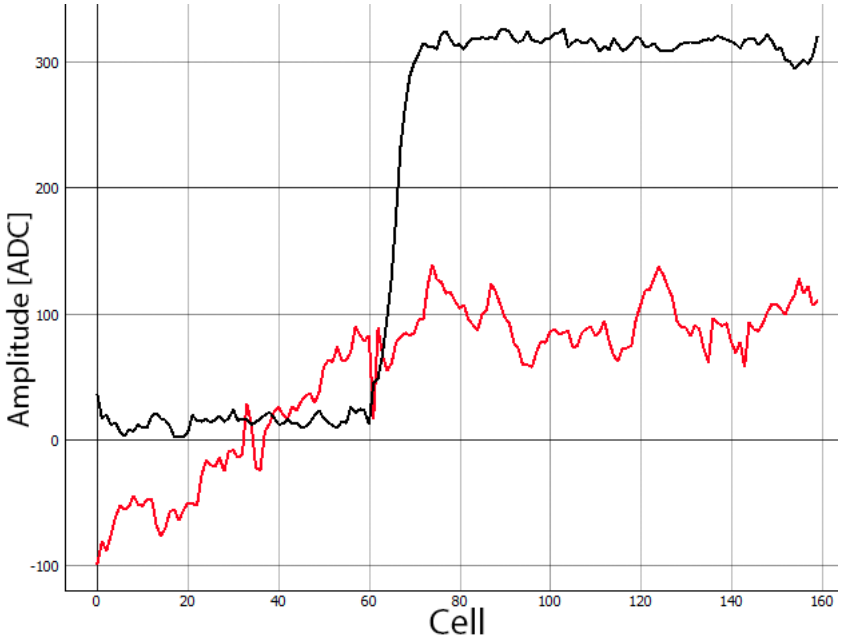

Figure 57 – Example of noisy cathode event. The cathode event is displayed in red, and anode event in black.

One other effect is a saturated cathode which is caused by a large surge of high energy events absorbed by multiple pixels, which is likely caused by cosmic background noise. An example is depicted in figure58. The saturated cathode channel will last a few events as depicted in figure 59 until the cathode discharges. Events with saturated cathodes are filtered out as all events with C/A-ratio above one are excluded.

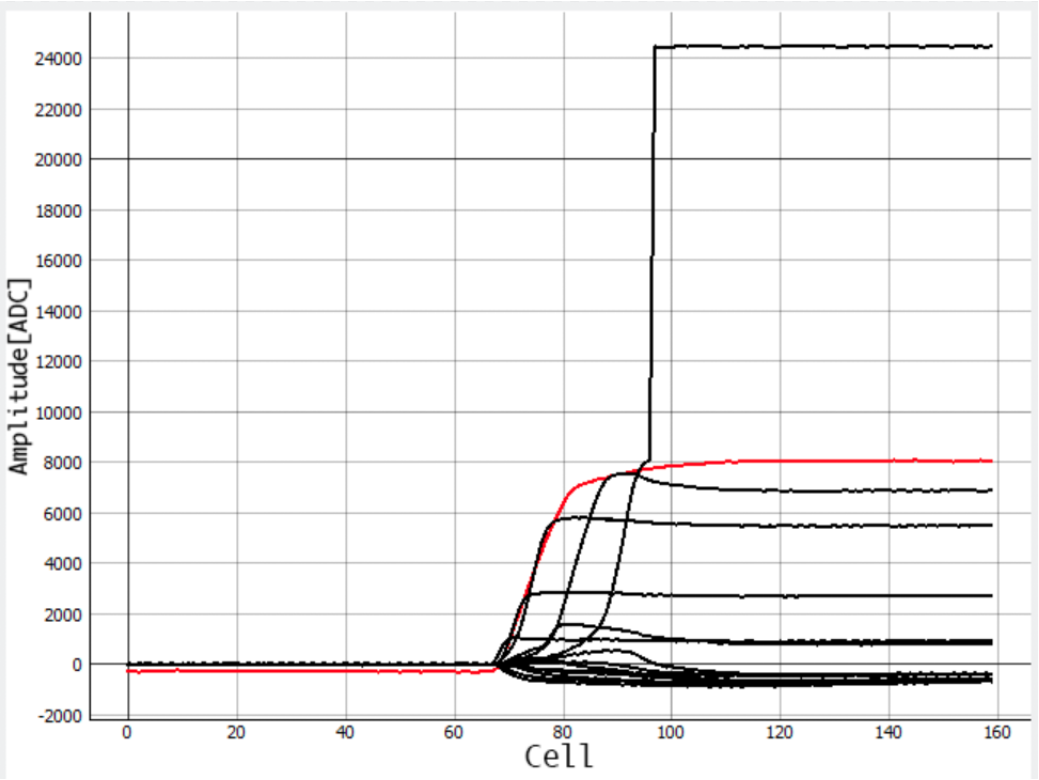

Figure 58 – An example of a large surge of high energy over multiple pixels which is likely caused by cosmic background noise.

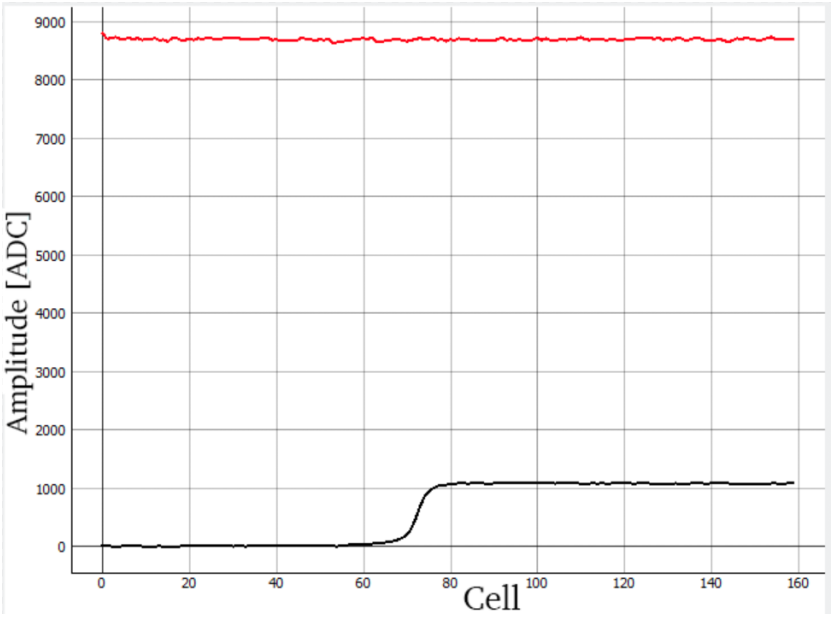

Figure 59 – An example of an event when the cathode channel is saturated.

The spectra before and after depth correction is depicted in figure 60. The FWHM is improved from 1.020% to 0.880%.

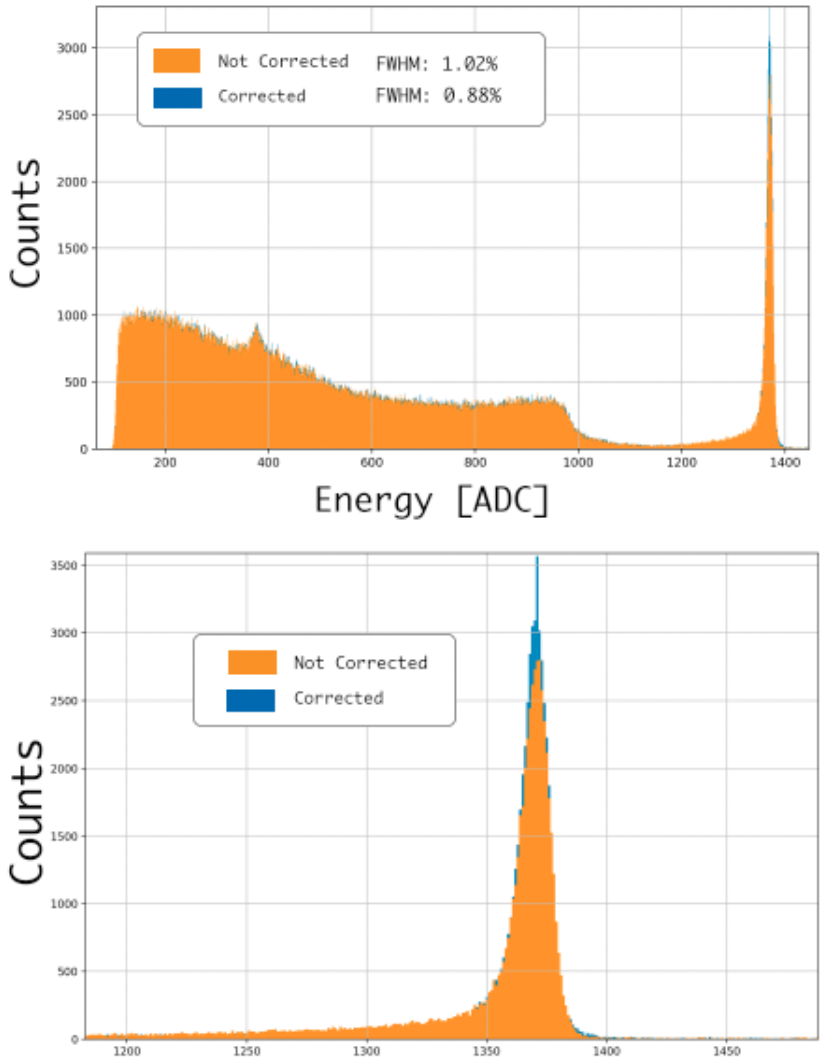

Figure 60 – Left: comparison of the raw data from single interaction events (orange) and the same data with depth correction using C/A-ratio(blue).Right: zoomed in peak of the same spectrum.

7.1 Discussion

An improvement of 0.14% is significant, however the validity of this result is questionable. As seen from figure 60 there is a prominent peak in one bin that differs from the raw data. This might be an effect caused by a binning-error and not the correction itself. If this peak is excluded, the FWHM of the depth corrected spectrum is 0.949%.

The cathode noise is the largest contributor to depth interaction uncertainty. As found in section 6.3 the cathode noise introduces significant amount of noise when the high voltage is connected, which translates to high uncertainty of the signal amplitude estimate, and thus C/A ratio fluctuations. Further development should include optimization of cathode signal pulse-height filter, and further investigation of how to minimize cathode noise within the hardware.

8 Conclusion

The *GDS-100 Calibration User Interface* has been successfully implemented. The user interface is implemented with *Python* library PyQt5. It is able to read data as it is logged from the IDEAS *Testbench* to create a close to "real-time" readout. The Interface is able to display spectra from each channel and a main spectrum with either single or multiple interaction events. For the single interaction event spectrum, the users are able to select which channels to be added, such as only selecting pixels with a specific spectral resolution or only depict corner and edge pixels. There is also the option to view data in detail by visualizing one single event. Suggested further development is to include categorizing of Compton scattering and charge sharing.

A proposed calibration routine is implemented within the interface which consist of characterizing and correcting variation in baseline levels and gain. Two different gain correction calculation methods were proposed: by internal calibration pulse and by channelspectra peak alignment. The internal calibrating pulse degraded the final spectral resolution. The second method produced a single interaction spectrum of Cs^{137} with a FWHM: 0.775%. Multiple interaction event spectra of Cs^{137} resulted in FWHM: 2.72%. Further development should include neighbor readouts with optimization signal pulse-height filter.

Efforts were made to improve spectral resolution by depth correction using C/A-ratio, which resulted inn an improvement of raw data from 1.020% to 0.880%. Further improvement should include depth interaction of multiple interaction events using drift time as well as exploring subpixel resolution. Further development to optimize the cathode pulse-height filter and investigation of minimizing cathode noise within the hardware was also suggested.

References

[1] Sofia O. K. Godø,
The Taming Of The Skew:A Calibration Routine For A Radiation Detector
Norwegian University of Science and Technology, 2020

[2] Julie E.McEnery
All-sky Medium Energy Gamma-ray Observatory: Exploring the Extreme Multimessenger Universe,
https://asd.gsfc.nasa.gov/amego/
NASA/GSFC, 2019

[3] Glenn F.Knoll,
Radiation Detection and Measurement,
John Wiley & Sons, 2rd. Edition, 1989

[4] Zhong He,
Review of the Shockley-Ramo theorem and its application in semiconductor gamma-ray detectors.
Nuclear Instruments and Methods in Physics Research A 463 (2001) 250–267

[5] P.Fõdish, M. Berthel, B. Lange, T.Kirschke, W. Enghardt, P. Kaever,
Charge-sensitive front-end electronics with operational amplifiers for CdZnTe detectors
JINST 11 (2016) T09001

[6] Ben G.Streetman, Sanjay Kumar Banerjee,
Solid State Electronic Devices
Pearson Education Limited, 7th Edition, 2016

[7] Feng Zhang,
Events Reconstruction in 3-D position Sensitive CsZnTe Gamma-Ray Spectrometers,
Ph.D. dissertation, University of Michigan, 2005.

[8] Zhong He,
1-D position sensitive single carrier semiconductor detectors.
Nuclear Instruments & Methods A, 1996. 380(1-2): p. 228-231.

[9] Glenn F.Knoll,
Radiation Detection and Measurement,
John Wiley & Sons, 2rd. Edition, 1989, p.115-116

[10] Jackson, John David (1999),
Classical Electrodynamic.
(3rd ed.). John Wiley & Sons. p. 43. ISBN 978-0-471-30932-1.

[11] Glenn F.Knoll,
Radiation Detection and Measurement,
John Wiley & Sons, 2rd. Edition, 1989, p.814-815

[12] Dan Xu,
Gamma-Ray Imaging and Polarization Measurement Using 3-D Position-Sensitive CdZnTe Detectors.,
Ph.D. dissertation, University of Michigan, 2005.

[13] P Christillin,
Nuclear Compton scattering,
Journal of Physics G: Nuclear Physics, Volume 12, Number 9

[14] Weiyi Wang, Willy R. Kaye, Jae Cheon Kim, Feng Zhang, Zhong He,
Improvement of Compton imaging efficiency by using side-neighbor events
IEEE Nuclear Science Symposium Conference Record, Knoxville, TN, 2010, pp. N41-144.

[15] Carlo Tintori,
WP2081 Digital Pulse Processing in Nuclear Physics,
CAEN Nuclear Physics, 2008.

[16] Valentin T. Jordanov, Glenn F.Knoll
Digital Synthesis of Pulse Shapes in Real Time for High Resolution Radiation Spectroscopy,
Nuclear Instruments and Methodes in Physics Research A 345 (1994) 337-345

[17] A. P. Demptster, N.M. Laird and D. B. Rubin,
Maximum Likelihood from Incomplete Data via the EM Algorithm
Journal of the Royal Statistical Society, Series B. 39 (1): 1–38. JSTOR 2984875. MR 0501537.

[18] Yuefeng Zhu,
Digital Signal Processing Methods for Pixelated 3-D Position Sensitive Room-Temperature Semiconductor Detectors,
Ph.D. dissertation, University of Michigan, 2012.

[19] Feng Zhang, William R. Kaye, Zhong He,
Performance of 3-D position sensitive CdZnTe detectors for gamma-ray energies above 1 MeV,
2009 IEEE Nuclear Science Symposium Conference Record (NSS/MIC), Orlando, FL, 2009, pp. 2012-2016, doi: 10.1109/NSSMIC.2009.5402137.

[20] Lloyd, Stuart P. (1957),
Least square quantization in PCM,
Bell Telephone Laboratories Paper. Published in journal much later: Lloyd, Stuart P. (1982). "Least squares quantization in PCM" (PDF). IEEE Transactions on Information Theory. 28 (2): 129–137.

[21] Multi Threading Library,
`https://docs.python.org/3/library/threading.html`

[22] Panda Library,
`https://pandas.pydata.org/about/`,

[23] pyqt5 Library,
`https://pypi.org/project/PyQt5/`

[24] *PyQtGraph*,
`http://www.pyqtgraph.org/`

Appendices

A Datapacket Header

Log format:

field	packet type	sequence flag	packet count	timestamp	data length	source id	trigger type	hold delay	channel type	trigger flag	x addr	y addr	cell pointer	cell data
size	8 bits	2 bits	14 bits	32 bits	16 bits	8 bits	8 bits	16 bits	8 bits	8 bits	8 bits	8 bits	8 bits	16 bits x 160
note	Always D9			working		0 for now	0 for now	dummy data	0x00 if cathode, 0x01 if anode, 0xFF if unknown					dummy data

Figure 61 – Datapacket header from the GDS-100 system.

B Circuit Diagram

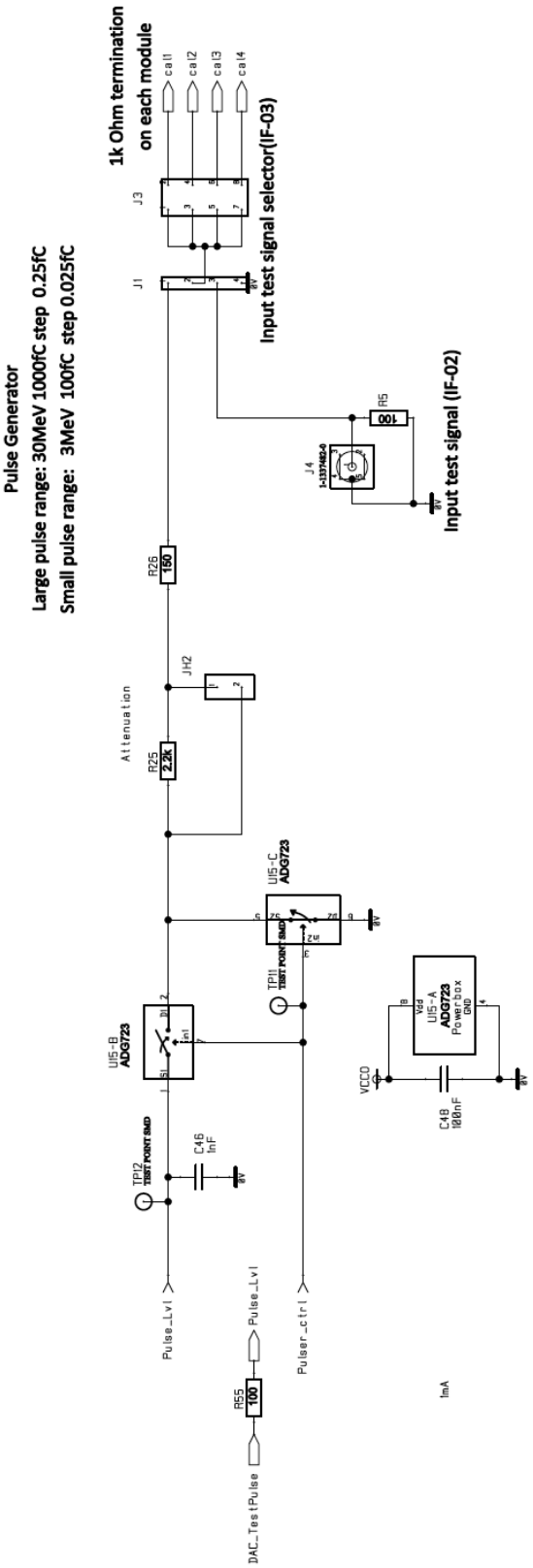

Figure 62 – Complete circuit of the internal calibration test pulse generator.

C Testbench Scripts

```
import sys
import time

#Make sure all test and triggers are off

#Create file for readout and enable
tb.newDataLogFile('gain_cal_100_la.bin')
tb.enableDataLogging(True)

#test on
tb.setAsicConfigBitFieldByAddr(139,1,0)

#cal pulse amplitude
tb.writeSysReg(0x0D05,2000)
#set amount for readout
tb.writeSysReg(0x0C02,100)
#forced readout of
tb.writeSysReg(0x0F07,0)

start = 1975
start_trig = 1325
for i in range(128):
    if i == 9:
        continue
    bit_address = start + i
    trig_bit_address = start_trig + i

    tb.setAsicConfigBitFieldByAddr(bit_address,1,0)
    tb.setAsicConfigBitFieldByAddr(trig_bit_address,0,0)
    tb.writeSysReg(0x0F00,0)
    tb.writeReadAsicConfig(0)
    time.sleep(1)
    tb.writeSysReg(0x0F00,1)
    #time.sleep(1)#check this!!
    #execute
    tb.writeSysReg(0x0C00,1)
    time.sleep(30)
    tb.setAsicConfigBitFieldByAddr(bit_address,0,0)
    tb.setAsicConfigBitFieldByAddr(trig_bit_address,1,0)
```

Figure 63 – Testbench script for automating internal calibration pulse readout for all channels.

```
import sys
import time
#config settings for readout:
#tb.writeReadAsicConfig(0)
tb.setAsicConfigBitFieldByAddr(26,1,0)
#RO_ALL
tb.setAsicConfigBitFieldByAddr(254,1,0)
#RO4B
tb.setAsicConfigBitFieldByAddr(158,1,0)

#send config
tb.writeReadAsicConfig(0)

#Create file for readout and enable
tb.newDataLogFile('pedestals.bin')
tb.enableDataLogging(True)

num_pulse = 10000
tb.writeSysReg(0x0C03, 400)#should be by default
tb.writeSysReg(0x0C04, 15999999)
#set maxchannels
tb.writeSysReg(0x0F05,130)
#set amount for readout
tb.writeSysReg(0x0C02,num_pulse)
#cal pulse amplitude
#tb.writeSysReg(0x0D05,0)
#set forced readout
tb.writeSysReg(0x0F07,0)
print('readout in process')
#execute
tb.writeSysReg(0x0C00,1)
```

Figure 64 – Testbench script for acquiring baseline data from each channel.

D System Settings

Table 5 – System Settings for Cs^{137} measurements

Paramter	**Setting**
Source	Cs137
Threshold, VTHR	2200
High Voltage, detector bias HV	-2500V
Clk Frequency	50Mhz
Readout frequency	6.25MHz
Read mode	Read neighbors = False
SH-DELAY	80
Trans-Impedance Amplifier Gain (TIA)	100[mV/mA]
Trigger Type	2
VFP	500
VFP0	2000
Gain pre-amplifiers	Gain_C3B

Table 6 – System Settings for Na^{22} measurements

Paramter	**Setting**
Source	Na22
Threshold, VTHR	2200
High Voltage, detector bias HV	-2500V
Clk Frequency	50Mhz
Readout frequency	6.25MHz
Read mode	Read neighbors = False
SH-DELAY	80
Trans-Impedance Amplifier Gain (TIA)	100[mV/mA]
Trigger Type	2
VFP	500
VFP0	2000
Gain pre-amplifiers	Gain_C3B

NTNU

Norwegian University of
Science and Technology